



Review

The Advanced Applications of 2D Materials in SERS

Yansheng Liu ^{1,*} , Zhenle Qin ¹, Junpeng Deng ¹, Jin Zhou ¹, Xiaobo Jia ¹, Guofu Wang ¹ and Feng Luo ^{2,*} 

¹ School of Microelectronics and Materials Engineering, Guangxi University of Science and Technology, No.2, Wenchang Road, Liuzhou 545616, China

² Tianjin Key Lab for Rare Earth Materials and Applications, Center for Rare Earth and Inorganic Functional Materials, School of Materials Science and Engineering & National Institute for Advanced Materials, Nankai University, Tianjin 300350, China

* Correspondence: yansheng.liu@gxust.edu.cn (Y.L.); feng.luo@nankai.edu.cn (F.L.)

Abstract: Surface-enhanced Raman scattering (SERS) as a label-free, non-contact, highly sensitive, and powerful technique has been widely applied in determining bio- and chemical molecules with fingerprint recognitions. 2-dimensional (2D) materials with layered structures, tunable optical properties, good chemical/physical stabilities, and strong charge–transfer interaction with molecules have attracted researchers' interests. Two-D materials with a large and flat surface area, as well as good biocompatibility have been considered promising candidates in SERS and widely applied in chemical and bio-applications. It is well known that the noble metallic nanostructures with localized surface plasmon effects dominate the SERS performance. The combination of noble metallic nanostructure with 2D materials is becoming a new and attractive research domain. Until now, the SERS substrates combined with 2D materials, such as 2D graphene/metallic NPs, 2D materials@metallic core-shell structures, and metallic structure/2D materials/metallic structure are intensely studied. In this review, we introduce different kinds of fabrication strategies of 2D and 3D SERS substrates combining with 2D materials as well as their applications. We hope this review will help readers to figure out new ideas in designing and fabricating SERS substrates with high SERS performance that could enlarge the applicable domains of SERS.

Keywords: SERS; 2D materials; metallic nanostructures; localized surface plasmon resonance



Citation: Liu, Y.; Qin, Z.; Deng, J.; Zhou, J.; Jia, X.; Wang, G.; Luo, F. The Advanced Applications of 2D Materials in SERS. *Chemosensors* **2022**, *10*, 455. <https://doi.org/10.3390/chemosensors10110455>

Academic Editors: Shan Cong and Chunlan Ma

Received: 30 September 2022

Accepted: 30 October 2022

Published: 2 November 2022

Publisher's Note: MDPI stays neutral with regard to jurisdictional claims in published maps and institutional affiliations.



Copyright: © 2022 by the authors. Licensee MDPI, Basel, Switzerland. This article is an open access article distributed under the terms and conditions of the Creative Commons Attribution (CC BY) license (<https://creativecommons.org/licenses/by/4.0/>).

1. Introduction

In 1922–1923, a wavelength-shifted scattering phenomenon was discovered [1]. In 1928, a paper about “a new radiation” which was based on the light scattering effect was published by professor C V Raman [2,3]. Nowadays, this “new radiation” has been well known as the Raman effect. In the Raman scattering process, the incident light interacts with the molecules by exchanging energy with vibrations modes of the molecules, and the collected scattering light carries the vibrational information that is unique for a molecular. Therefore, the Raman spectrum with the collecting of the information of Raman active vibrations modes provides a fundamental qualitative analysis method (molecular identification). Further, the Raman intensity has a linear relation with the number of the molecules and this relationship is widely applied in quantitative analysis [4,5]. Although Raman scattering is important, several disadvantages have restricted its application, such as weak intensity, very low cross-section, fluorescence background, and inefficient collection of scattering light [6–10]. As an inelastic light scattering process, only one in 10^6 – 10^8 photons illuminating the sample can undergo Raman scattering, and the rest of the photons go competitive ways, such as fluorescence, Rayleigh elastic scattering, and heating [11]. These instinctive properties of Raman scattering have limited its analysis efficiency and applicability. Due to such inefficiency of Raman scattering, finding a method of enhancing signals of Raman spectroscopy is a long-term pursuit.

About 46 years ago, Fleischmann with his colleagues found that the Raman signal of pyridine was enhanced on rough silver electrodes [12]. Afterward, surface-enhanced Raman scattering (SERS) as a new research domain has been enormously studied. Until now, tens of thousands of research papers have been published about the physical theory of SERS or fabrications of the high-sensitive SERS substrates [13]. SERS as a surface-sensitive technique makes Raman a powerful technology for detecting biology and chemistry with high sensitivity and selectivity [12,14–18]. Currently, SERS is considered the only method which could be applied in simultaneously detecting a single molecule and providing its chemical fingerprint [6,19–22]. By applying the SERS substrates, reasonable and clear Raman spectra could be obtained under the low laser intensity condition without unexpected Raman line which is caused by laser heating.

In the study of SERS, metallic nanostructures play crucial roles in enhancing SERS signals [20]. The metallic nanostructures can generate light-induced oscillation of conduction electrons which is known as surface plasmon resonance [23]. Plasmon excitation leads to strongly enhanced electromagnetic fields near the nanoparticle surfaces which can induce large electromagnetic fields resulting in enhanced Raman signals [6,24]. As a result, molecules adsorbed near the electromagnetic hot spots dominate the Raman signal up to 10^8 or more [8,24,25]. Due to their larger light-induced electromagnetic field, kinds of metallic nanostructures with strong plasmonic properties as excellent SERS active systems have been widely explored [26,27], such as Au NPs [28–31], Au pillars [32], Au nanorod [33,34], Au disc [6,35], Au nano-hole [36–39], nano-pillar [32], Ag NPs [28] and Au nano-pyramid [27,40].

The finding of 2D material starts a new research domain in SERS. Two-D materials possess some unique distinct chemical and physical properties, such as a layered structure and the optical bandgap related to the number of layers. The large surface area of 2D materials with a variety of chemical compositions provides more efficient SERS activity sites. By designing and applying metallic nanostructures combined with 2D materials, the flat surface of 2D material provides more possibility of absorbing the target molecules through Van der Waals force. The chemical bond of 2D materials provides strong charge transfer resulting in an enhanced SERS performance. The few atomic thicknesses of 2D materials generate a small bandgap between coherent metallic nanostructures and induce strong plasmon effects which dominate the SERS sensitivity. Therefore, the combination of 2D materials with plasmonic metallic nanostructures is a promising method to get high-performance SERS substrates.

In this review, SERS substrates combined with different 2D materials such as graphene, h-BN, BP, SnSe₂, MoS₂, and WS₂ are illustrated. Through this review, we hope it may help readers to figure out some new interesting categories in fabricating 2D materials-based SERS substrates with high performance.

2. Mechanism of SERS: CM and EM

For SERS, two mechanisms are widely accepted: electromagnetic mechanism (EM) and chemical mechanism (CM) [6,19]. In the classical description of the Raman scattering process, the dipole in a molecule is induced by the oscillating electric field, and this light-induced dipole radiates scattered light with changing energy with molecule vibrations [41–43]. The strength of light-induced dipole moment P can be described in an equation: $P = \alpha E$ where α is the polarizability scales, and E is the strength of the light-induced electric field. Based on such theory the electromagnetic field plays an important role in enhancing the signal of Raman. For the EM, the enhanced Raman signal is caused by the localized electromagnetic field [44–46]. When the incident light illuminates the metallic structures at the wavelength of plasmon resonance frequency, ω , the amplitude of the electromagnetic field can be enhanced to $E(\omega)$. The molecules adsorbed at the surface of such metallic structures also is excited by an incident-induced electromagnetic field whose magnitude is E_0 . Then photon of the incident light interacts with the molecules and is scattered by an electromagnetic field $E(\omega')$ at the scattered light frequency of ω' . The

Raman scattering field, therefore, could be regarded as $E_R \propto E(\omega)E(\omega')$. For the normal Raman intensity, it is proportional to the square of incident-induced E_0 , which is $I_R \propto |E_0|^2$. For the SERS intensity, the scattered light-induced and the plasmon field both contributed to the SERS intensity which is $I_{\text{SERS}} \propto |E(\omega)E(\omega')|^2$. So, the SERS enhancement factor (EF) is $I_{\text{SERS}}/I_R \propto |E(\omega)E(\omega')|^2/|E_0|^4$. For low-frequency bands, the difference between $E(\omega)$ and $E(\omega')$ is very small. In such a case, we approximately consider the $E(\omega) \approx E(\omega')$. So, the $EF = |E(\omega)|^4/|E_0|^4$. In electromagnetic models, a molecule located near the metallic structure is regarded as a is considered as polarizable point dipole. When the plasma resonance wavelength λ_{LSPR} is equal to $1/2(\lambda_{\text{exc}} + \lambda_{\text{RS}})$ where the λ_{exc} is the excitation wavelength and the λ_{RS} is Raman scattering wavelengths, the SERS performance can be maximized [47–49]. To maximize the plasmon field, the best way is to excite the structure at the localized surface plasma resonance (LSPR) frequency. However, in most cases, the excitation light sources are fixed. In such a case, tuning the LSPR frequency closer to the excitation light frequency is an important way to get the highest plasmon field and larger SERS performance.

For the CM, it is mainly caused by charge transfer between target molecules and substrate, usually, it has an enhancement factor of 10–100 [20]. It is found that CM is mainly governed by the energy difference between the highest occupied energy level (HOMO) of the metal and the lowest unoccupied energy level (LUMO) of the molecule, and the EF scales roughly as $(\omega_X/\bar{\omega}_e)^4$, in which $\bar{\omega}_e$ is an average excitation energy between the HOMO of the metal and the LUMO of the molecule where ω_X is the energy between HOMO and LUMO of the free molecule [50]. Because the charge transfer needs less distance, CM is usually thought to be a “first layer effect”. It has been reported that the first monolayer molecules absorbed on substrate often illustrate higher SERS signal in comparison with the second layer [24]. The SERS effects of the first layer require a uniform and small rough surface.

3. Two-D Materials-Based SERS Substrates

3.1. Graphene

Graphene has attracted lots of interest since it was mechanically exfoliated from graphite [51–53]. Graphene as a 2D material with particular electrical, optical, mechanical, and thermal properties has been widely applied in SERS [19,54–59]. Owing to its gapless characters, graphene leads to a strong charge–transfer interaction between itself and molecules which results in the SERS enhancement. Graphene has been known as a fluorescein quencher which can efficiently reduce the fluorescein noise and improve the SERS spectra [60]. The π - π stacking interaction between molecules generates the chemical bond which makes graphene a molecules catcher resulting in an enrichment of molecules on the surface of graphene [51,61–63]. It has been reported that the EF for the single-layer graphene is 10–100 and the single-layer graphene has a higher Raman peak intensity compared to bilayer graphene [64,65]. Additionally, the graphene with a sub-nanometer thickness can act as a sub-nanometer spacer between metallic NPs which could induce extremely strong LSPR effects.

For pure graphene, it is already known that the SERS enhancement of molecules on the graphene surface within a range of 1–100 is induced by a typical CM in comparison with SiO_2/Si as a reference [22]. To achieve the goal of high SERS performance, the hybrid metallic NPs-graphene or the metallic nanostructures-graphene system is enormously studied [66–68]. There are mainly two methods available to fabricate Au or Ag NPs on graphene. In the chemical method, the precursors such as HAuCl_4 or AgNO_3 are applied to form metallic NPs with varying diameters through reduction reactions [29,69]. In the physical method, the hemispherical or spherical NPs with different diameters are generated by annealing the thin metal film. Due to the easy fabrication process, graphene-metallic NPs are widely studied. For the metallic NPs-graphene SERS substrates, normally, the flat graphene surface is considered to contribute to a larger SERS enhancement. However, the situation seems not simple. In the study of Weigao Xu [7], the graphene was transferred on

top of the half-spherical Au particles to form graphene/hemispherical Au nanoparticles SERS substrate (Figure 1a). By applying a flat graphene film on top of metallic nanostructures, the Raman signal of copper phthalocyanine as an analyte was enlarged. On the contrary, in the study of Weigao Xu [30], the bent graphene surface showed stronger Raman enhancement than the flat graphene surface (Figure 1b). In his study, the graphene was directly transferred on top of target metallic NPs, and then an annealing process was applied which was called the “active” process. By applying the annealing process, graphene was not flat anymore and stick to the spherical surface of nanoparticles tightly. Through such an “active” process which the author mentioned, the SERS performance was enhanced around 2 times (Figure 1a). Why do the opposite situations occur? By comparison, the distance between NPs and the diameter of the NPs affected a lot. For the homogeneous and large gap nanostructured substrates, a flat graphene surface is needed to absorb more molecules around the edge of the metal structures. And for the un-uniform and small bandgap nanostructures, the flat graphene surface can let the molecules far from the “hot spots” induced by the small bandgap of adjacent nanostructures. So, the nature of surface-dependent graphene-NPs SERS performance is related to the morphology of the metallic structures. In the design and fabrication 2D materials-based SERS substrates, the gap between NPs or metallic nanostructures and their diameter should be taken into account.

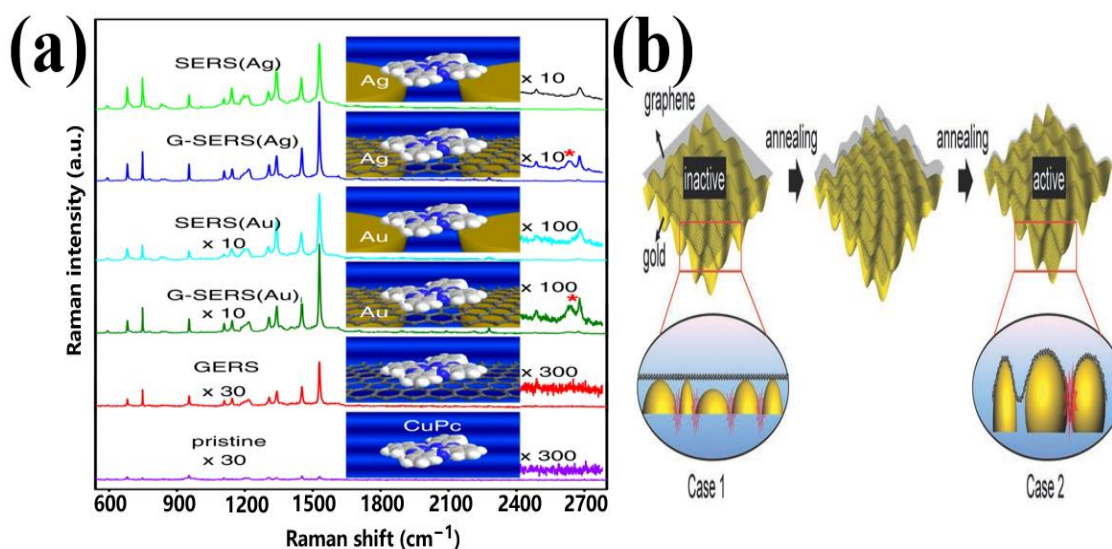


Figure 1. (a) Comparison of the SERS spectra of CuPc molecules on Ag NPs, graphene-Ag NPs, Au NPs, graphene-Au NPs, graphene and pristine CuPc, respectively. Reprinted from Ref. [7] with permission of 2012 Proceedings of the National Academy of the Sciences. (b) Schematic illustration of graphene-veiled SERS substrates with graphene spread over the curved side of Au nano-islands in two cases. Case 1 (SERS-inactivity) and case two (SERS activity) were the cases before and after an activation process of thermal annealing, respectively. Reprinted from Ref. [30] with permission of 2013 Wiley Online Library.

Except for the NPs/graphene SERS system, the metallic nanostructures with kinds of morphologies attract lots of research interest and are intensely studied. In comparison with randomly generated metallic NPs, the nanostructures with controllable morphologies and uniform diameters can lead to more spatially stable SERS spectra which are extremely important in quantifying the number of analytes in SERS [70]. In the work of Zhao Xing [71], the graphene/gold nanorods vertical array (G/GNRs-VA) hybrid substrate was fabricated (Figure 2a). The gold nanorod vertical array was fabricated through the seed-mediated growth method [72] (Figure 2b,c), and the graphene was transferred on top by using the wet transfer method (Figure 2d,e). The G/GNRs-VA substrate showed a limit of detection (LOD) of 10^{-13} M and an EF of 7.9×10^8 by using R6G as the analyte. The graphene/nano-

disk (Figure 2f) and graphene/nano-holes (Figure 2g) structures have been studied by Qingzhen Hao [39]. When the graphene was introduced, the nanostructure substrates combined with graphene showed enhancements around 3-fold or 9-fold using MB as an analyte in comparison with the bare nanohole or nanoparticle substrates, respectively. Graphene-Au nanopyramid structure (Figure 2h,i) was investigated by Pu Wang [27]. He demonstrated a graphene-Au nanopyramid heterostructure to detect dopamine and serotonin with LOD down to 10^{-10} M. The SERS EFs for dopamine and serotonin were 2×10^8 and 2×10^9 , respectively. The graphene/Au Triangular Nanoarrays (G/TNAs) system (Figure 2j) was studied by Xingang Zhang [73]. By applying graphene, it efficiently improved the thermal stability of noble metal Triangular Nanoarrays. The G/TNAs substrate can be reused around 16 times without significant SERS intensity loss.

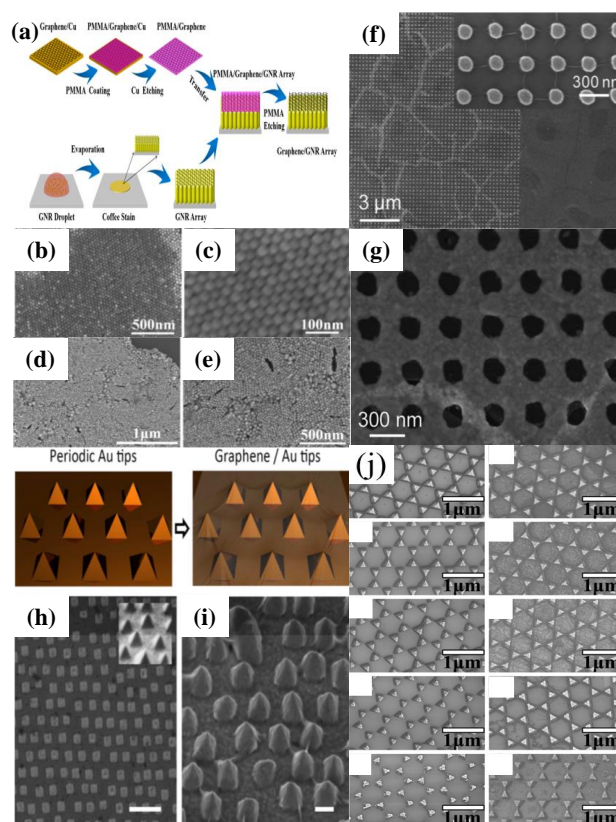


Figure 2. (a) The scheme of fabrication of G/GNRs-VA hybrid substrate. (b,c) SEM images of GNRs-VA. (d,e) SEM images of G/GNRs-VA. Reprinted from Ref. [71] with permission of 2019 Elsevier. (f) SEM images of graphene/nano-disk structures. (g) SEM images of graphene/nano-holes structures. Reprinted from Ref. [39] with permission of 2012 American Chemical Society. (h) SEM images of Au nanopyramid structure. (i) SEM images of graphene-Au nanopyramid structure. Reprinted from Ref. [27] with permission of 2015 American Chemical Society. (j) the Au TNAs (left column) and G/TNAs (right column) structures, respectively. Reprinted from Ref. [73] with permission of 2017 American Chemical Society.

Normally the plane SERS structure generates “hot spots” in the XY plane, and its SERS performances are contributed by the gaps between horizontal patterns or the edge effects of the structures. The SERS performance of simple plane structures is usually restricted by the limited density of the hot spots [74,75]. To get high-performance substrates, the architecture of SERS substrates grows in the Z dimension is a promising method. The constructed three-dimensional (3D) structures can make use of vertical dimensions and generate LSPR in the vertical gaps could enlarge the SERS performance. For such architecture, 2D materials play an important role in generating atomic vertical bandgaps as a spacer between metallic nanostructures. The sub-nanoscale gap in the horizontal dimension between

the coherent nanostructures could largely enhance the SERS performance. In the study of Xuanhua Li [76], graphene was applied as a nano-spacer from the metal film–metal nanoparticle coupling system (Figure 3a). Graphene was transferred on top of 100 nm-thickness Ag film, and Ag NPs were deposited on top of graphene through a thermal evaporation process (Figure 3b). By introducing the graphene, an atomic gap between the Ag NPs and Ag film was formed which were regarded as “hot spots”. In this structure, the Ag NPs themselves, Ag NP-Ag NP, and Ag NP-Ag film have strong electromagnetic fields. By analyzing the SERS performance of the proposed 3D structures which use the R6G as the analyte. Remarkably, the Ag NPs-graphene-Ag film system exhibited an enhancement ratio of about 1700 than normal graphene. This enhancement was nearly 115 times and 14 times larger than the Raman intensity of graphene/Ag film and graphene/Ag NPs systems, respectively (Figure 3c). A similar strategy was applied by Hongki Kim [77] in which the single Au nanowire/graphene/Au film system (Figure 3d–f) was fabricated. In his study, graphene played a role of a sub-nanometer spacer between the nanowire and the Au film. The EF of a single nanowire on the graphene platform was calculated to be 1.18×10^6 in which Cu-phthalocyanine (CuPc) was applied as an analyte.

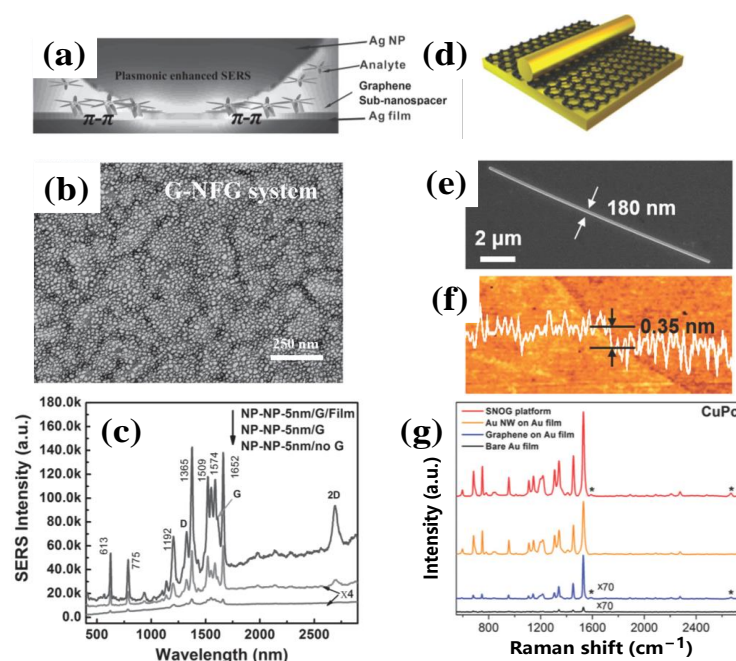


Figure 3. (a) The scheme of Ag NPs/graphene/Ag film structure. (b) The SEM image of Ag NPs/graphene/Ag film structure. (c) The SERS spectra of R6G molecules on Ag NPs/graphene/Ag film, Ag NPs/graphene, and Ag NPs. Reprinted from Ref. [76] with permission of 2014 Wiley Online Library. (d) The scheme of Au NW/Au film structure. (e) The SEM image of Au NW/Au film structure. (f) The AFM image of Au NW/Au film structure. (g) The SERS spectra of CuPc molecules on single Au NW/graphene/Au film (SNOG), Au NW/Au film, graphene/Au film, and Au film, respectively. The asterisk-marked peaks denote G and 2D bands of graphene. Reprinted from Ref. [77] with permission of 2016 Royal Society of Chemistry.

Except for the metal NPs/graphene/metallic film system, the metallic NPs/graphene/discontinuous metal film are investigated. In comparison with the metal film underneath, the discontinuous metal film provides more edges or sharp points that can improve the SERS enhancement performance. In the study of Yuan Zhao [46], the 3D hybrid system with monolayer graphene sandwiched between silver nanohole arrays and gold nanoparticles (Figure 4a) was fabricated. The nanohole structure was fabricated by using the EBL method, and the Ag was deposited on top of the holey structure to form the Ag nanoholes (Au Hs) structure (Figure 4b,c). The graphene was transferred on top of the Ag nanoholes structure, and the Au NPs as deposited on top of the graphene by thermally

treating a thin Au film. The proposed Au NPs/graphene/Ag NHs (Figure 4d,e) structure exhibited ultrahigh SERS sensitivity with a LOD down to 10^{-13} M. A similar structure was Ag NPs/bilayer graphene/Au nanonet structure (Figure 4f) which has been fabricated by Chonghui Li [78]. In his study, Ag NPs/bilayer graphene/Au nanonet was proposed to form the dense 3D hot spots (Figure 4g–i). The gap in the nanonet structure was around 8.67 nm. The CVD-grown bi-layer graphene with a theoretical thickness of 0.64 nm was transferred on top of the Au nanonet structure through a wet transfer process to generate an ultrasmall gap between Au NPs and Au nanonet structures. This substrate has been applied in detecting R6G and crystal violet (CV) with LODs of 10^{-13} and 10^{-12} M respectively. In our previous paper, the porous Si_3N_4 films were applied as masks to form the periodic Au nano-discs (Au NDs) with varying diameters. By transferring single-layer graphene on Au NDs and fabricating Au NPs on top of graphene, the 3D Au NPs-graphene-Au NDs structures were synthesized. Through such structure, the graphene defects and non-defects induced Raman signals both were enlarged. By analyzing the two kinds of Raman intensity ratios above mentioned and applying the linear graphene defects models, we quantify the defects crystalline of CVD-grown graphene [37].

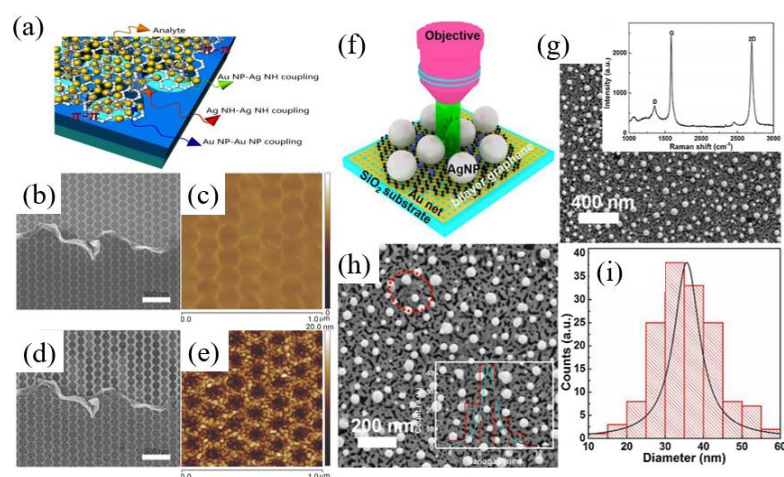


Figure 4. (a) The scheme of Ag NPs/graphene/Ag NHs structure. (b,c) The SEM image and the AFM images of graphene/Ag NHs structure. (d,e) The SEM image and the AFM images of Ag NPs/graphene/Ag NHs structure. Reprinted from Ref. [46] with permission of 2017 Royal Society of Chemistry. (f) Schematic illustration of Ag NPs/bilayer graphene/Au nanonet SERS composite substrate. (g) SEM image of Ag NPs/bilayer graphene/Au nanonet SERS samples. Inset: The Raman spectrum of graphene. (h) The high-magnification SEM image of Ag NPs/bilayer graphene/Au nanonet SERS samples. (i) Size distribution of 150 Ag NPs counted from (h). Reprinted from Ref. [78] with permission of 2018 Elsevier.

Another interesting 3D SERS system is NPs/graphene/NPs. Due to the different chemical stability of different metals, the hybrid NPs/graphene/NPs systems combining two kinds of metals were important in SERS. The Ag NPs/graphene/Au NPs system with 3D hot spots (Figure 5a) was investigated by Chao Zhang [55]. The Au NPs and Ag NPs were both generated by annealing the thin metal films which were deposited on either side of graphene (Figure 5b–g). For this structure, the LOD for R6G and CV were 10^{-11} and 10^{-12} M respectively. Except for the pure metallic NPs, the AuAg alloy NPs also was studied. In the study of Qingyan Han [79], the 3D AuAg alloy NPs/graphene/AuAg alloy NPs structure (Figure 5h,j) was investigated in which the AuAg alloy NPs were synthesized by using mixed HAuCl_4 and AgNO_3 as precursors (Figure 5i,l). By changing the concentration ratio of HAuCl_4 and AgNO_3 , the absorbance of AuAg alloy NPs could be tuned. The 3D structure was fabricated layer by layer where the AuAg alloy NPs film was self-assembled in a single layer and graphene was transferred by using the wet transfer method (Figure 5m,n). By optimized the ration of Au/Ag ($\text{HAuCl}_4/\text{AgNO}_3 = 1/3$), 3D

AuAg alloy NPs/graphene/AuAg alloy NPs structure showed a LOD of 10^{-9} M using R6G as an analyte.

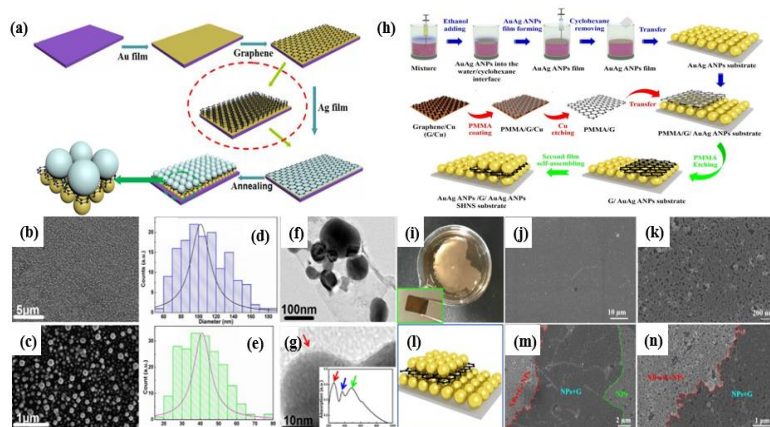


Figure 5. (a) Scheme illustration of the preparation process for Ag NPs/graphene/Au NPs structure. (b,c) The SEM image of Ag NPs/graphene/Au NPs structure. (d,e) Diameter distribution of Ag NPs and Au NPs. (f) TEM image of the Ag NPs/graphene. (g) TEM image of graphene/Au NPs (Insert: the absorption spectrum of Au NPs/graphene/Au NPs. Reprinted from Ref. [55] with permission of 2018 Elsevier. (h) Schematic illustration of the preparation process for the AuAg NPs/graphene/AuAg NPs structure. (i) Picture of formatting monolayer AuAg NPs film on water/cyclohexane interface. (j,k) Different magnification SEM image of single-layer AuAg NPs array on Si substrate. (l) Schematic diagram of AuAg NPs substrate. (m,n) The low and high-magnification SEM images of AuAg NPs/graphene/AuAg structure formed on Si substrate. Reprinted from Ref. [79] with permission of 2020 Royal Society of Chemistry.

3.2. Hexagonal-Boron Nitride (h-BN)

Like graphene, a hexagonal boron nitride (h-BN) sheet is another atomic-thick 2D material. It is well known that the h-BN possesses excellent thermal stability even at high temperatures up to 800 °C in oxidative environments [80]. Due to the unique surface properties, h-BN can be modified by kinds of organic groups such as hydroxyl, alkoxy, amino, and amine which make h-BN a universal substrate for “clamping” metallic NPs as EM “hot spots”. Due to its unique properties, it has been reported the h-BN could prevent the oxidation of Ag NPs which efficiently increases the stabilities of Ag NPs/h-BN SERS substrate [81]. In the study of Na-Yeong Kim, the h-BN/Ag NPs and Au NPs/h-BN/Ag NPs were fabricated and studied [81]. The h-BN sheet was directly transferred onto the Ag NPs by using a dry transfer process which also was widely used in transferring exfoliated graphene. By dispersing the collid Au NPs solution, he synthesized the Au NPs/h-BN/Ag NPs sandwich structure with atomic gaps (Figure 6a). From the SEM image of Ag NPs before and after the transfer h-BN sheet, it was clear that the monolayer h-BN was successfully transferred on top of Ag NPs (Figure 6b,c). The prepared Au NPs/h-BN/Ag NPs illustrated an excellent SERS performance with an EF of 9.35×10^7 and an LOD of 10^{-12} M in detecting R6G (Figure 6d). The h-BN/Ag NPs system was also studied by Dipankar Chugh with high NPs tensity [82]. The metal NPs were deposited on Si/SiO₂ by using e-beam evaporation, and the h-BN layer was transferred on top of the NPs through a wet transfer technique (Figure 6e). The topography image of the h-BN/Ag NPs sample was obtained by SEM and AFM measurements (Figure 6f–h) which illustrated a successful transfer process. In his research, the h-BN/metallic NPs showed stronger SERS performance than bare metallic NPs (Figure 6i) which revealed the superior adsorption capabilities of h-BN layers over metallic NPs. The thickness depended SERS performance of h-BN covered Au NPs system was studied by Gwangwoo Kim [83]. In his research, the SERS performance h-BN/Au NPs systems using CVD grown and mechanically exfoliated h-BN with different thicknesses were studied (Figure 6j,k). By controlling the layer number

of h-BN, the optimized thickness of h-BN for h-BN/Au NPs system was 7 nm for the exfoliated h-BN and five-layer-thickness for CVD grown h-BN. Normally, the thicker h-BN showed a potential of absorbing a larger number of molecules on its surface which cause a larger EF of SERS. However, in h-BN/Au NPs systems the thickness-dependent behavior was mainly affected by the gap between the Ag NPs which affected the EM around the surface of h-BN. When increasing the thickness of h-BN to 7 nm, the maximum of the EM of Ag NPs can be optimized at the fixed gap distance between Ag NPs (Figure 6l,m).

Except for the chemistry applications, the h-BN also has been applied in biology. In the study of Jia Liu [84], the h-BN nanosheets synthesized by chemical and mechanical exfoliation methods (Figure 6n,o) were applied as a novel system in real-time monitoring CuPc labeled microRNA through the SERS technique. In his research, the CuPc as an important molecule in the photodynamic therapy process was real-time monitored by using the h-BN nanosheets as the SERS substrate. In comparison with SiO₂, h-BN nanosheets exhibited higher SERS performance (Figure 6p,q). Through the amplification of the SERS enhancement caused by h-BN nanosheets, the LOD of CuPc labeled miRNA-21 reached 0.7 fM in live cells. This h-BN platform illustrated a promising way of early monitoring and guiding the early therapy, realizing tumor elimination (Figure 6r).

3.3. Black Phosphorus (BP)

Black phosphorus (BP) as a member of 2D materials has attractive physical properties for high-performance chemical sensing applications. Compared with graphene or MoS₂, BP has superior molecular adsorption energy [85,86]. Recently, black phosphorus (BP) has attracted a lot of scientists' interest due to BP's unique semiconducting properties. The BP possesses extremely high hole mobility of $10^4 \text{ cm}^2 \text{ V}^{-1} \text{ s}^{-1}$ is larger than graphene [87], and its in-plane anisotropy with puckered orthorhombic structure provides an opportunity of designing conceptual devices and applications [88–90]. BP has a strong near-infrared (NIR) absorption and possesses a high efficiency of photothermal conversion that makes it an ideal candidate in efficient NIR photothermal cancer therapy and photoacoustic bioimaging [91–93]. BP nanosheet as a 2D material is a novel nanocarrier and photosensitizer with efficient generation of singlet oxygen for chemotherapy and photodynamic therapy [94–96]. Due to its biodegradability, intrinsic photoacoustic properties, and biocompatibility, the main application of black phosphorus is in bio-therapy, such as cancer theragnostic [97], chemo-photothermal therapy [91], photothermal therapy, photodynamic therapy, drug delivery [96]. Among these applications, the BP-NPs systems play an important role as a SERS substrate to reveal the bio-reaction in the cell or real-time monitor the therapy. In the research of Henan Zhao [98], the BP-Au NPs system has been fabricated and applied to investigate the intracellular behaviors (Figure 7a). By reducing the HAuCl₄, the Au NPs can be modified on BP sheets (Figure 7b–d). The SERS experiments were carried out by applying human hepatocellular carcinoma (HepG2) cells as the model. By applying the BP-Au NPs SERS substrate, the enhanced Raman signals can be observed which gave more details inside the cell and rich fingerprint information of the intracellular biological components. Through label-free SERS images (Figure 7e–g), the endocytosis mechanism of the cell using BP-Au NSs was revealed. The plasmon effect of the BP-Au NPs system not only acts as a SERS sensor in the human body but also acts as a Photothermal therapy (PTT) nano-agent applied in cancer therapy [99]. The BP-Au NPs system has been applied in breast cancer treatment in vitro and in vivo by Guangcun Yang and achieved the desired therapeutic outcome (Figure 7h). The BP-Au NPs structure has a stable lamellar structure (Figure 7i,j), good biocompatibility and photostability which were capable of producing sufficient hyperthermia which makes it a suitable and novel PTT nano-agents for cancer therapy. In vitro and in vivo experiments demonstrated that PTT was mediated by BP-Au nanosheets and exhibited more effective therapeutic efficacy than that based on pure BP nanosheets. During this process, the therapeutic effect in vivo was real-time monitored by the SERS technique. Through the photographs of tumor tissue (Figure 7k,m) and the SERS spectrum (Figure 7l,n), they showed that photo-thermolysis destroyed the

membrane microstructure of cancer cells and caused the intracellular redistribution of the nanocomposites [99].

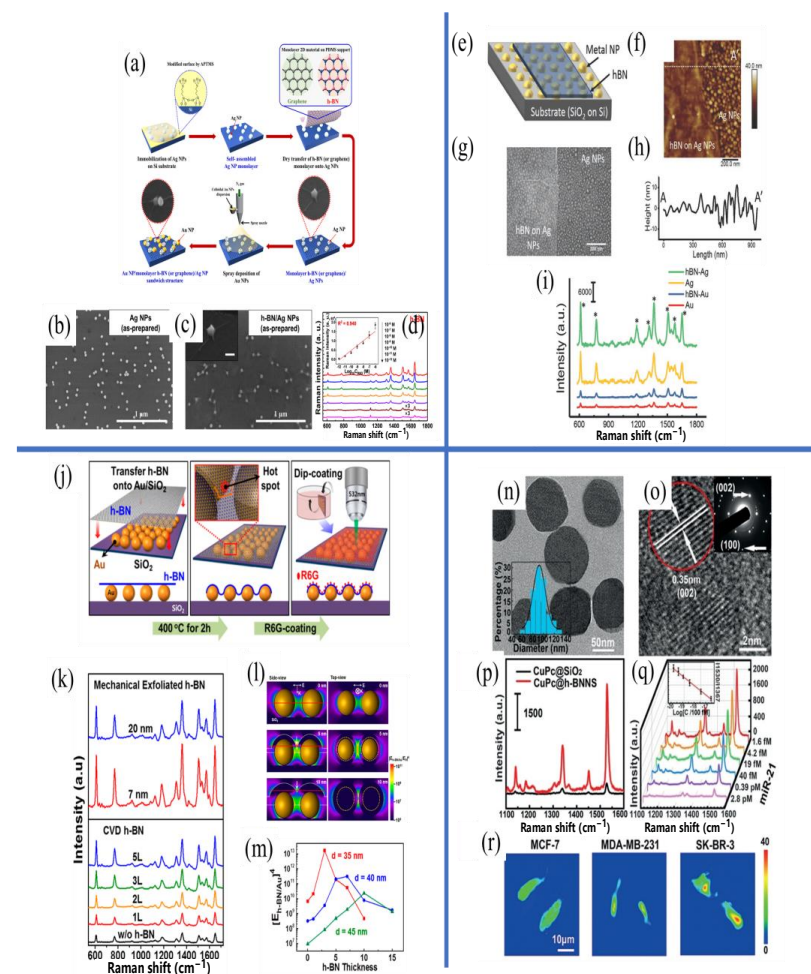


Figure 6. (a) Schematic illustration of the procedure for fabricating h-BN/Ag NP substrates and Au NP/h-BN/Ag NP sandwiched substrates. (b,c) SEM images of prepared Ag NP with or without h-BN covered. (d) Au NP/h-BN/Ag NP substrates with various molecular concentrations of R6G from 10^{-6} to 10^{-12} M. Reprinted from Ref. [81] with permission of 2019 American Chemical Society. (e) Schematic illustration of the h-BN/Ag SERS sample. (f,g) AFM and SEM images of h-BN/Ag SERS sample. (h) AFM line scan showing height variation along the white line marked in (f). (i) Representative Raman spectra for 10^{-3} M R6G obtained from h-BN and non-h-BN covered Au and Ag samples. The plots are offset vertically for clarity. Reprinted from Ref. [82] with permission of 2019 Wiley Online Library. (j) Schematic Illustration of Shell-Isolated SERS process on an h-BN/Au/SiO₂ substrate. (k) h-BN thickness-dependent SERS measurement of R6G on an h-BN/Au/SiO₂ substrate with layer numbers of h-BN from 0 to 5 layers. (l) Side-view and top-view simulation images (left and right columns, respectively) of EM field distribution on the h-BN (0, 5, and 10 nm)/Au/SiO₂ substrate (diameter of Au = 30 nm, bandgap = 40 nm, laser wavelength = 532 nm, incident E-field = 1 V/m). The position of the top-view simulation is marked by the red line in the side-view image. The h-BN film is marked by the white dotted line in the side-view image. (m) Plot of maximum EM field and h-BN thickness in the h-BN/Au/SiO₂ substrate with different bandgap values (35, 40, and 45 nm). Reprinted from Ref. [83] with permission of 2016 American Chemical Society. (n) TEM image of h-BN nanosheets. Inset: corresponding size-distribution histograms of h-BN nanosheets. (o) High-resolution TEM image of h-BN nanosheets. Inset: selected-area electron-diffraction pattern (SAED). (p) SERS effects of CuPc on SiO₂ and h-BNNS. (q) SERS spectra of intracellular miR-21 with CuPc@HG@BN. Inset: I_{1530}/I_{1367} versus intracellular quantity of miR-21. (r) Raman mappings. Reprinted from Ref. [84] with permission of 2019 Wiley Online Library.

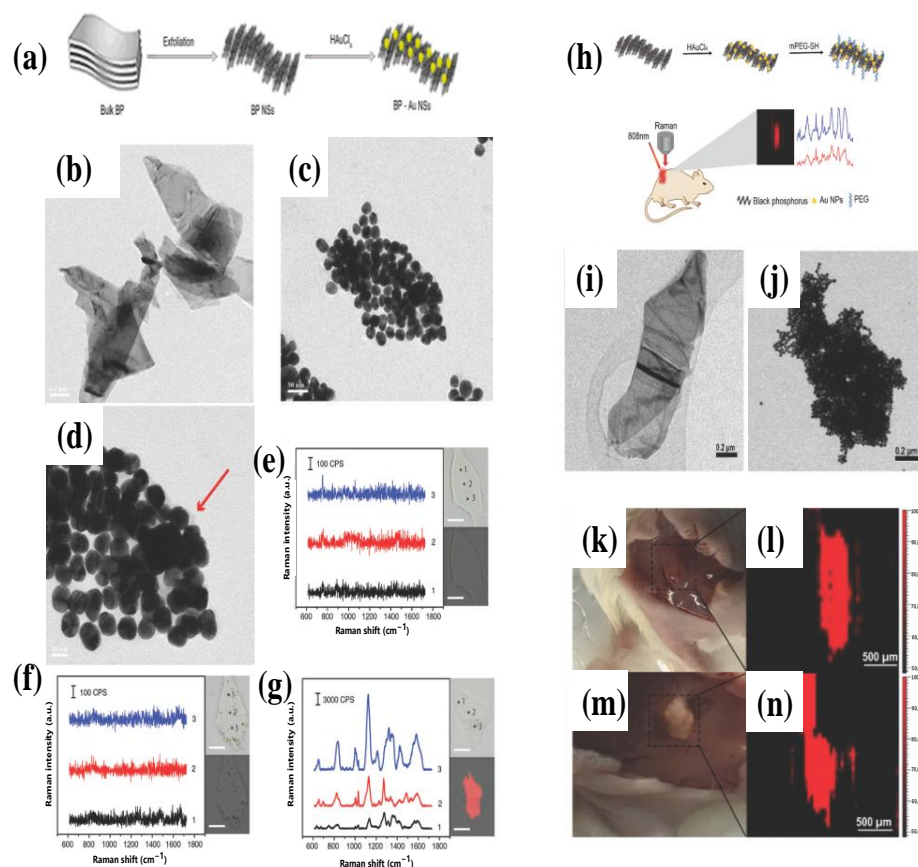


Figure 7. (a) Schematic illustration of synthetic process of BP-Au nanosheets. (b) TEM image of BP nanosheets. (c,d) Overall and enlarged TEM images of BP-Au NPs nanosheets. (e) Raman mapping and corresponding spectra of HepG2 cells incubated with (e) fresh medium. (f) BP nanosheets and (g) BP-Au NPs. Reprinted from Ref. [98] with permission of 2018 Walter De Gruyter. (h) Schematic illustration of the fabrication of BP-Au nanosheets and biomedical applications. (i,j) TEM image of BP sheets and BP-Au NPs nanosheets. (k,m) Photographs of tumor tissue injected with BP-Au NSs before and after NIR laser irradiation. (l,n) SERS images of tumor tissue injected with BP-Au NSs before and after NIR laser irradiation. Reprinted from Ref. [99] with permission of 2017 Royal Society of Chemistry.

3.4. SnSe_2

For the Raman scattering of the bio-molecules, the UV light is much easier to excite them and cause a larger polarization of biomolecules [100]. Besides, the UV light is much close to the electron transition spectrum which causes a strong Raman resonance and a separation of Raman spectra far from its fluorescein background region. Normally, due to the plasmon damping by inter-band transitions in the UV region only a few metals such as Rh [101,102], Ru [101], Rd [103], Co [104], copper [104], Al [105], and Pb showed the SERS performance in UV region.

Two-D-layered Tin Diselenide (SnSe_2) nanoflakes with an indirect bandgap with a bulk bandgap of approximately 1.0 eV have strong absorption in the UV region [106,107]. The biology molecules adsorbed on SnSe_2 could generate large SERS enhancements under UV light excitation (Figure 8a). For instance, the LOD of CV molecules adsorbed on SnSe_2 nanoflakes could reach a concentration as low as 10^{-7} M [100]. For the SnSe_2 flake, the band structure is caused by the thickness that affects the SERS performance (Figure 8b). When the bandgap between the conduction band (CB) and valence band (VB) of the multi-layer SnSe_2 match the vibrational state of the molecular (Figure 8c), the charges transfer between multilayer SnSe_2 and molecules which results in the enhancements of the Raman signal (Figure 8d).

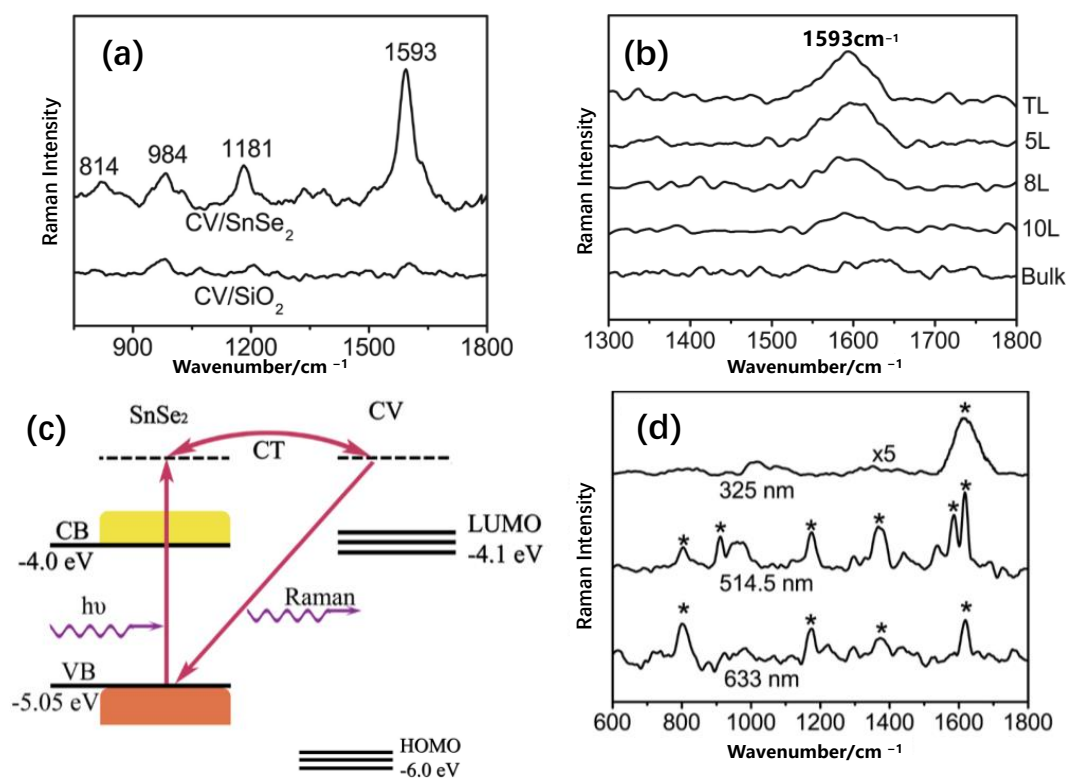


Figure 8. (a) Raman spectra of the CV molecules (10^{-4} mol/L) on the blank SiO₂/Si substrate and SnSe₂ substrates. All of the Raman signals were excited by a 325 nm laser. (b) Raman spectra of CV molecules (10^{-6} mol/L) on the SnSe₂ substrate with different thicknesses. (c) The energy level and charge–transfer process diagram of triple layers SnSe₂ nanoflakes and CV molecules. (d) Comparisons of the UV–SERS signals of CV (10^{-6} mol/L) on the SnSe₂ substrate with 632.8, 514.5, and 325 nm excitation. The Raman band for CV was marked by a star (*). Reprinted from Ref. [100] with permission of 2019 Wiley Online Library.

3.5. MoS₂

Molybdenum disulfide (MoS₂) as a new type of 2D-layered transition metal dichalcogenides has been widely applied in SERS. MoS₂ possesses lots of unique electronic, optical and mechanical properties. The mechanisms of SERS of graphene and MoS₂ are different. Graphene is a gapless semiconductor with a nonpolar C–C bond [108,109] which induces strong charge transfer. Unlike graphene, MoS₂ is a semiconductor with both the top and bottom surface of the Mo atoms layer bonded by the sulfur atoms to generate a covalent Mo–S band with the polarity in the vertical direction to the surface. Due to such essential properties, both weak charge transfer and dipole–dipole coupling of MoS₂ may occur and contribute to the SERS [80,110]. It has been observed that the pristine MoS₂ (P-MoS₂) flake does not show any SERS enhancements, and the MoS₂ flake with defects showed SERS enhancement. When using the oxygen-plasma treated MoS₂ (OT-MoS₂) or argon-plasma treated MoS₂ (AT-MoS₂) nanoflakes, the SERS performance of the MoS₂ could be enhanced by more than 1 magnitude. For the plasmon-treated MoS₂ flake, the defects which are introduced in the T-MoS₂ flake change the local surface properties of MoS₂ flakes. The plasma-generated “holes” in the 2D MoS₂ flake create the local dipoles which give rise to the enhanced Raman signals of molecules absorbed in such region. Further, the site of the defeat of the MoS₂ flake could absorb the oxygen or H₂O molecules in ambient air resulting in doped holes in the MoS₂ flake. These doped sites also enhance the charge transfer process between the molecules and the MoS₂ flake resulting in enhanced Raman signals [111]. To get high SERS performance, the categories of combining MoS₂ with metallic NPs or metallic nanostructures are promising ways in enhancing the SERS performance of MoS₂-based SERS substrates. The Au NPs modified exfoliated MoS₂ substrates (Figure 9a)

were fabricated by Shao Su [112]. By controlling the concentration of precursors, the Au NPs@MoS₂ SERS substrates with a varying number of Au NPs were fabricated (Figure 9b,c) with tunable optical absorption (Figure 9e). The optimized Au NPs@MoS₂ system exhibited an EF of 8.2×10^5 and a LOD of 8.2×10^{-7} M in detecting R6G. In the study of Renu Rani [113], the monolayer MoS₂ was cut by low-power focused laser-cutting, and the Au NPs were drop-casted on top of MoS₂ forming the Au-MoS₂ substrate (Figure 9f). The edge of the MoS₂ attracts major of the Au NPs due to the strong electrovalent bond between Mo and S atoms (Figure 9g–i). Through the Raman mapping image, it revealed the larger SERS performance existed around the edge of the MoS₂ with the aggregated Au NPs (Figure 9j,k). The SERS LOD of such substrates in detecting dye molecules could reach 10^{-10} M, and the EF was 10^4 .

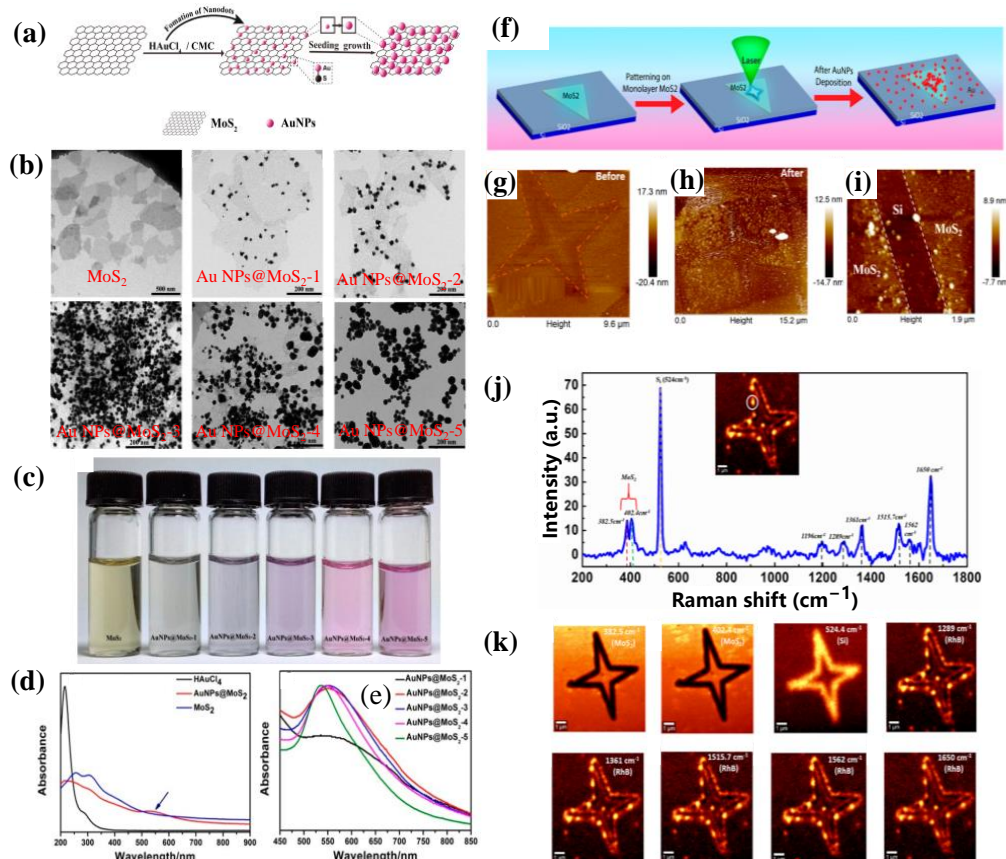


Figure 9. (a) Schematic illustration of synthesizing Au NPs@MoS₂ nanocomposite. (b) TEM images of MoS₂ and five kinds of Au NPs@MoS₂ nanocomposite with different numbers of Au NPs named from Au NPs@MoS₂-1 to Au NPs@MoS₂-5. (c) Photo images of MoS₂ nanosheets and different Au NPs@MoS₂ nanocomposite. (d) UV–vis spectra of MoS₂, HAuCl₄, and Au NPs@MoS₂ nanocomposite. (e) UV–vis spectra of different Au NPs@MoS₂ nanocomposite. Reprinted from Ref. [112] with permission of 2014 American Chemical Society. (f) Schematic graphics demonstrate the nanopatterning of monolayer MoS₂ by laser irradiation, followed by AuNP deposition. (g,h) AFM topography image of MoS₂ sheet before and after the decoration of AuNPs on the SiO₂/Si substrate, showing the distribution of AuNPs on the 2D MoS₂ flake. (i) Magnified view of the Au NP decorated the artificial edge of the MoS₂ sheet, where the white dotted lines indicate the outlines of the laser-etched edges. (j) Raman peaks of RhB dye (denoted black dotted line) along with characteristic signals of MoS₂ (red and green dotted line) and Si (yellow dotted line), acquired at the edge of the nanostructure (white marked circle in inset panel). (k) Raman mapping images of a star-shaped feature at signature peaks of MoS₂, Si and RhB depicting the formation of localized hotspots along the artificial edges of the star-shaped nanostructure. Reprinted from Ref. [113] with permission of 2020 American Chemical Society.

Except for the application of MoS₂ films, the MoS₂ with interesting morphologies which were synthesized by using chemical methods illustrated excellent SERS performance when combining with plasmon structures. The spherical or flower-like MoS₂ synthesized by using chemical methods is attracted researchers' interest and is widely applied in SERS. MoS₂ nanosphere (Figure 10a–c) and Au NPs-MoS₂ nanosphere system (Figure 10d–g) were studied by Hengwei Qiu, and they illustrated extremely high SERS performance (Figure 10h,i) [114]. The MoS₂ nanospheres were fabricated via using molybdenum ions sulfuration reaction proceeding. After modifying Au NPs using HAuCl₄ as a precursor, the coherent Au NPs with few nanometer gaps provided a huge electromagnetic field resulting in an extremely large EF of SERS (Figure 10p). This structure showed LODs of 10⁻¹⁴ M for R6G and 10⁻¹⁵ M for MB. Jaspal Singh used hexa-ammonium heptamolybdate tetrahydrate and thiourea as precursors to synthesize 3D MoS₂ nanoflowers (Figure 10j–o) with the tunable surface area for the application in photocatalysis and SERS-based sensing [115]. By comparison with the MoS₂ nanoflowers with varying surface areas, it revealed that the SERS performance showed a positive correlation with the surface area of MoS₂. Besides, the pure MoS₂ nanoflowers illustrated a LOD of 10⁻⁷ M in detecting RhB molecules (Figure 10p). Another method of fabricating MoS₂ nanoflower was introduced by Shib Shankar Singha [116]. The MoS₂ nanoflower was synthesized from MoO₃ (Figure 10q–s), and the Au NPs were then modified on the surface of MoS₂ nanoflower to form Au NPs-MoS₂-flowers structure (Figure 10t,u). The SERS LOD of Au NPs-MoS₂-flowers structure substrates could reach 10⁻¹² M using R6G as a probe molecule. The calculated EF was around 10⁹ in the detection of bilirubin molecules in comparison with bare MoS₂ NF substrate (Figure 10v,w).

3.6. WS₂

WS₂ as a typical member of the TMDs family possesses strong spin-orbit coupling and band splitting deriving from the d-orbitals of transition metal [117]. Also, WS₂ exhibited special advantages in spintronics and valleytronics [118,119]. In the study of Lan Meng [120], the CVD growth of WS₂ film as a substrate was studied. In comparison with the SiO₂/Si substrates, the Raman signal of R6G absorbed on the WS₂ surface was prominently enhanced. By adding the layer number, the band structure of WS₂ translates from direct to indirect bandgap. In such a case, the relaxation process changes from direct recombination to indirect recombination in which the excited electrons in a few-layer WS₂ or transfer from R6G molecules would stay a longer time.

The high-performance metallic nanostructure/WS₂ system is a promising candidate in SERS such as Ag@WS₂ QD nanocomposites [121] and Au NPs/WS₂ [122,123]. The 3D Au NPs/WS₂@Au NPs (Figure 11b,c) were synthesized by Zhengyi Lu [124] with a LOD of 10⁻¹¹ M. In this system, the bilayer WS₂ was directly growing on the surface of Au NPs which generate a core-shell structure (Figure 11a,d,e). The in-situ grown bilayer WS₂ film through a thermal decomposition process was applied as a precise nano-spacer. The electrical bandgap between metallic nanostructures in the vertical direction can achieve strong plasmonic coupling which induced a tremendously enhanced local electromagnetic field resulting in extremely amplified Raman signals (Figure 11f). The dense 3D hot spots in this hybrid plasmonic nanostructures provided more "hot spots" which were responsible for the extremely enhanced SERS performances. Besides, the tight protected Au NPs by WS₂ acted as a protection film that stabilized Au NPs/WS₂@Au NPs hybrid plasmonic nanostructures from oxidation and increases its reproducibility and reusability.

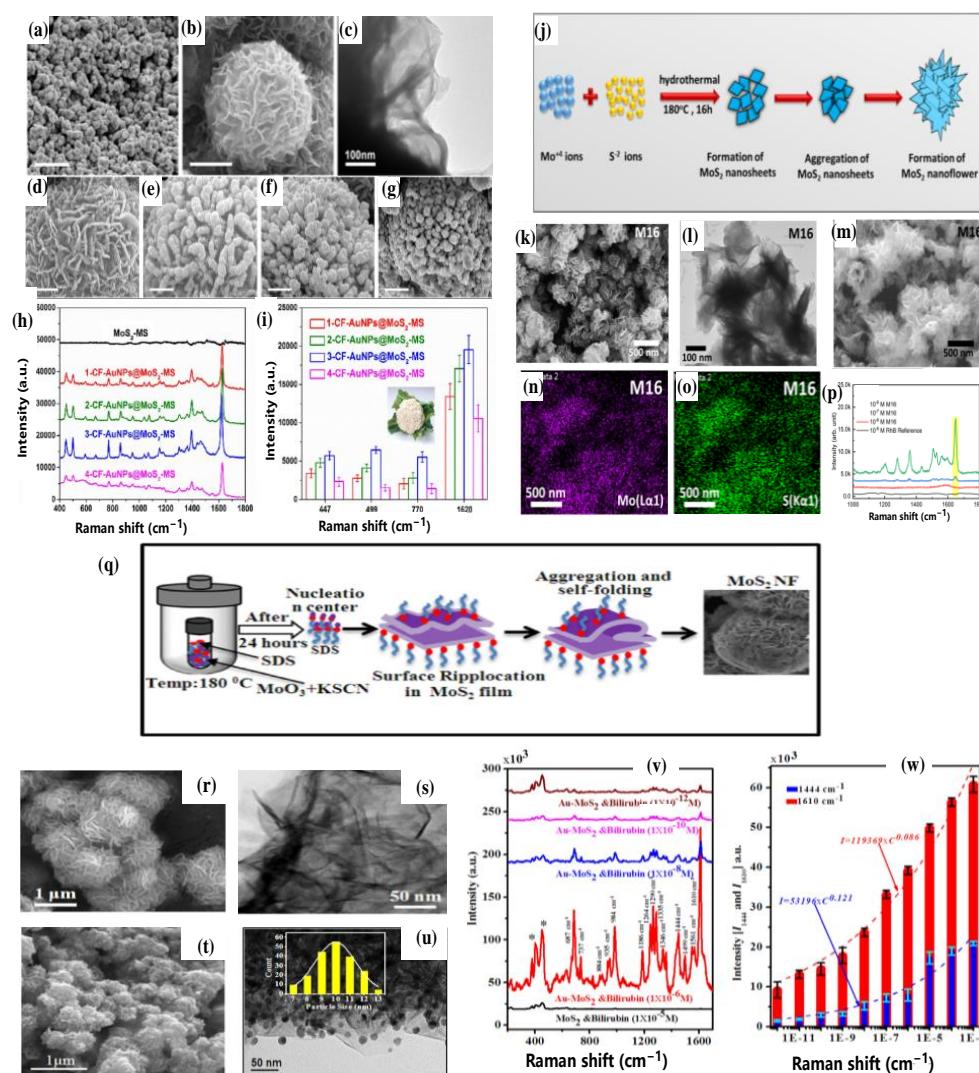


Figure 10. (a,b) FESEM image of hierarchical MoS₂ microspheres (MoS₂-MS) in low magnification. (c) TEM image of hierarchical MoS₂ microspheres. (d–g) SEM images of the AuNPs modified microspheres (Au NPs@MoS₂-MS) with different HAuCl₄ concentrations, respectively were (d) 1 mM, (e) 2 mM, (f) 3 mM, and (g) 4 mM. Scale bar: 200 nm. (h,i) SERS activity of the pure MoS₂-MS, 1-, 2-, 3-, and 4-CF-AuNPs@MoS₂-MS for MB detection (10^{−11} M). (g) Raman intensity at peaks of 447, 499, 700, and 1620 cm^{−1} for different composites in (h). Reprinted from Ref. [114] with permission of 2018 Elsevier. (j) Schematic diagram revealing the growth mechanism of MoS₂ nanoflowers. (k) SEM images showing the flower-like morphologies of the sample named M16. (l) TEM images of sample M16 revealing the flower like nanostructures consisting of 2D nanosheet-like structures. (m) SEM image of sample M16 showing the creation of MoS₂ nanoflower. (n,o) Elemental mapping of sample M16 display the uniform distribution of individual Mo and S atoms respectively. (p) Concentration dependence SERS spectra of RhB dye molecules with sample M16-based substrate. Reprinted from Ref. [115] with permission of 2020 Elsevier. (q) Schematic presentation of MoS₂ nanoflowers preparation using hydrothermal method. (r,s) SEM image and TEM image of MoS₂ nanoflowers. (t,u) SEM image and TEM image of Au-MoS₂ nanoflowers Inset of (u) shows the histogram of the size of Au NPs. (v) SERS spectra of R6G with concentrations ranging from 1 × 10^{−4} M to 1 × 10^{−12} M using MoS₂ (black curve), AuNP (dark yellow) and Au-MoS₂ substrate. Asterisk (*)-marked peaks are from the MoS₂. (w) Bar diagram depicting concentration vs intensity plot of 1358 cm^{−1} (I₁₃₅₈, blue bar) and 1535 cm^{−1} (I₁₅₃₅, red bar) modes of R6G. The blue and red dash lines were fitted curves according to the power law for modes 1358 cm^{−1} and 1535 cm^{−1}, respectively. Reprinted from Ref. [116] with permission of 2018 Elsevier.

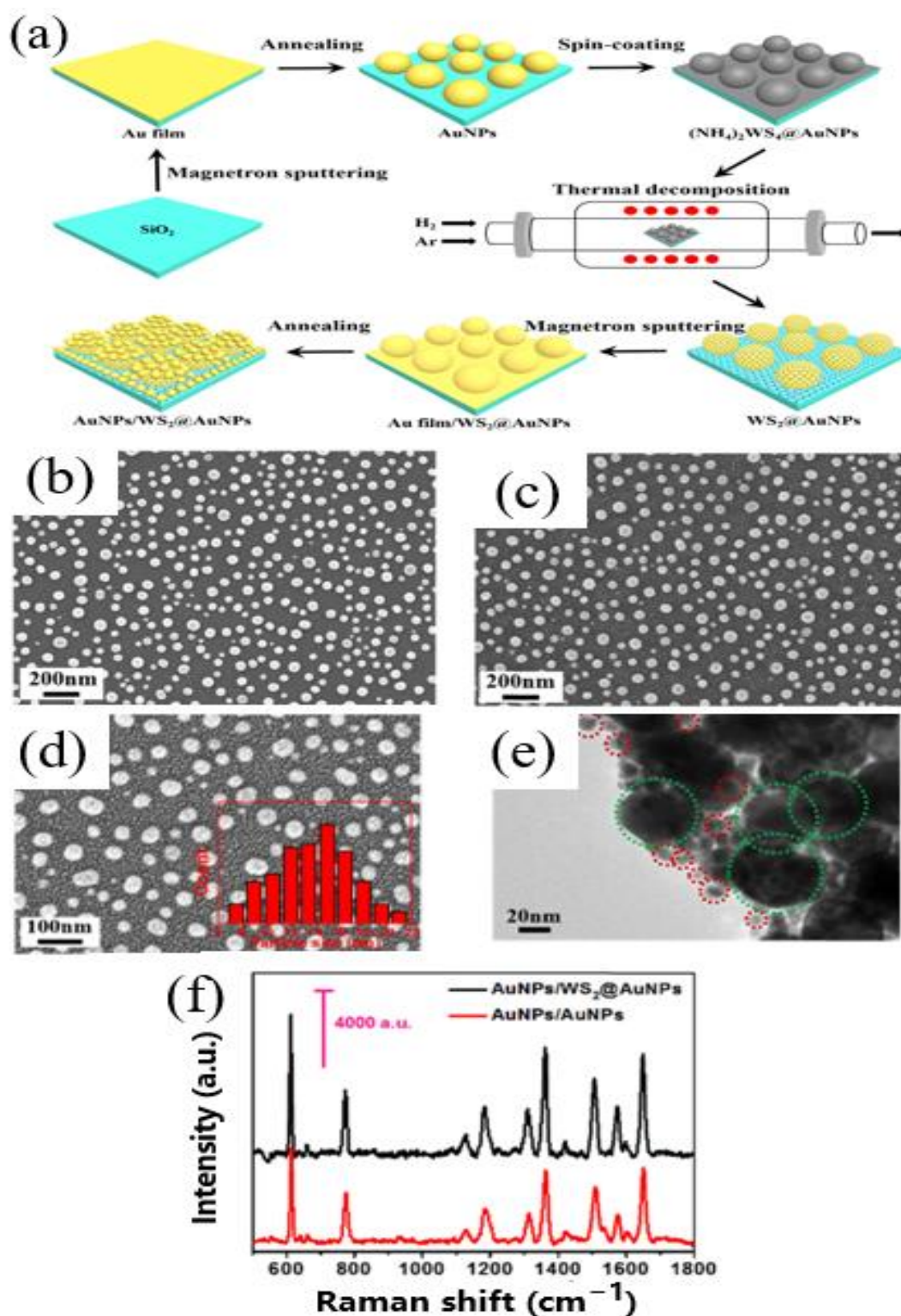


Figure 11. (a) Schematic illustration of synthetic process of Au NPs/WS₂@Au NPs hybrids. (b,c) SEM images of the Au NPs generated from annealing thin Au film and WS₂@Au NPs composites. (d) SEM images of Au NPs/WS₂@Au NPs. The inset pattern showed the size distribution of small Au NPs achieved through the annealing process of 3 nm Au film. (e) TEM image of the Au NPs/WS₂@Au NPs composites. The green and red dotted circles label the outline of Au NPs with different average diameters, respectively. (f) SERS spectra of R6G with a concentration of 10⁻⁵ M were collected from Au NPs/WS₂@Au NPs and Au NPs/Au NPs substrates. Reprinted from Ref. [124] with permission of 2018 Optical Society of America.

3.7. SERS Substrates with a Combination of Two Kinds of 2D Materials

The integration of two kinds of SERS substrates is an interesting way to get SERS substrates that illustrate higher SERS sensitivity than either one of them. The interaction between 2D materials layers plays a crucial role in enhancing SERS performance.

The Au NPs/2D MoS₂/graphene system (Figure 12a,b) was studied by Mohammed Alamri [125]. The SERS performance of MoS₂/graphene substrates did not show any enhancement in comparison with pure graphene substrate which was owned to weaker CM enhancement SERS performance. However, when Au NPs decorate on top of MoS₂/graphene substrates forming Au NPs/MoS₂/graphene system, the SERS performance was larger than Au NPs/graphene system (Figure 12a). This result was contributed by the interlayer coupling of MoS₂/graphene heterostructure. Besides, the distance between the Au atom and the S atomic consisting of layered MoS₂ also affected the SERS performance of Au NPs/2D MoS₂/graphene system. Through the FDTD simulation by varying the layer number of Au, it revealed that the EF could be affected by the distance between the Au atoms and S atoms. This modulation of distance at the subatomic level indeed played a critical role in further enhancing the EM effect. In the study of Samar Ali Ghopry [63], the Au NPs/WS₂ nano-dome/graphene van der Waals heterostructure (Figure 13a) was fabricated. In his study, the WS₂ nano-domes were directly grown on the surface by thermal treating (NH₄)₂WS₄ precursor, and Au NPs were fabricated on top of /WS₂ nano-dome/graphene through a thermal treating method of thin Au film (Figure 13b). In Au NPs/WS₂ nano-dome/graphene structure, both WS₂ nano-domes, and Au NPs illustrate the LSPR effect which is responsible for the Raman signal enhancement (Figure 13c). The LOD of Au NPs/WS₂ nano-dome/graphene van der Waals heterostructure can reach 1×10^{-12} M using R6G as an analyte (Figure 13d).

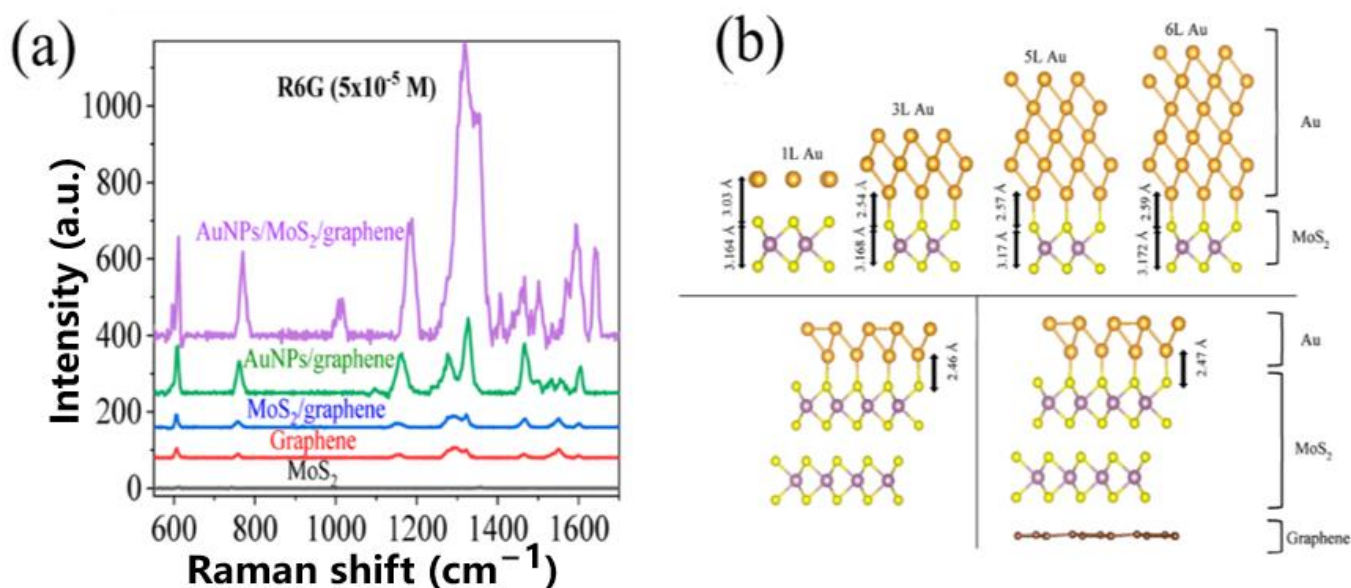


Figure 12. (a) R6G Raman spectra of 5×10^{-5} M concentration with different substrates: AuNPs/MoS₂/graphene (purple), AuNPs/graphene (green), MoS₂/graphene (blue), graphene (red), and MoS₂ (black). (b) (top) Atomic layer stacks of Au/MoS₂ hybrid heterostructures with different numbers of Au layers of 1L, 3L, 5L and 6L on monolayer MoS₂. The interface distance between the two materials is also illustrated. The atomic layer stacks of 2L Au/2L MoS₂: hybrid heterostructures (left-bottom) without graphene layer and (left-bottom) with graphene layer. Reprinted from Ref. [125] with permission of 2019 American Chemical Society.

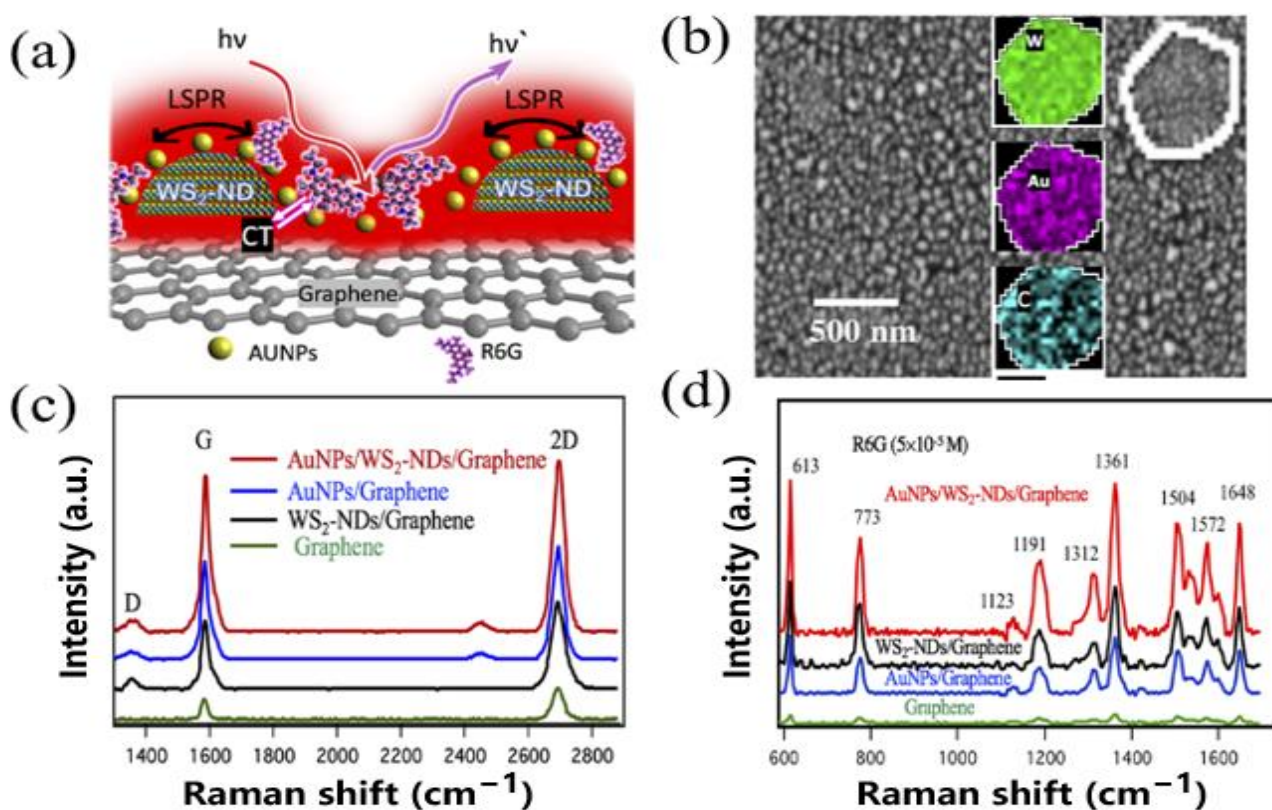


Figure 13. (a) Schematic design of the SERS substrate with AuNP/WS₂-ND/graphene van der Waals (vdW) heterostructure. (b) SEM image of an AuNP/WS₂-ND/graphene sample and EDS maps of W (green), Au (purple) and C (blue). (c) Raman spectra of graphene taken on four samples: graphene only (green), WS₂-ND/graphene (black), AuNP/graphene (blue) and AuNP/WS₂-ND/graphene (red) using a 488 nm a laser with a power output of 1 mW. (d) Raman spectra of R6G molecules at the concentration of 5×10^{-5} M deposited on Au NP/WS₂-ND/graphene (red), WS₂-ND/graphene heterostructure substrates (black), and AuNP/graphene (blue) with an excitation length of 532 nm. Reprinted from Ref. [63] with permission of 2020 American Chemical Society.

4. Comparisons of Applications of 2D Materials in SERS

Since the discovery of graphene, 2D materials have sparked an ever-growing interest due to their amazing physical and chemical properties. Leading to promising potential as high-quality flexible substrates. For example, h-BN, BP, SnSe₂, MoS₂ and WS₂ are new sorts of materials that can be used as substrates for SERS. The hybrid 2D materials/metal SERS platform provides additional advantages when combined with traditional plasmonic metal structures, including higher enhancement factors for SERS, oxidation protection of the metal surface and protection of the molecules from photo-induced damage. The following discussion will focus on the advantages, disadvantages, and limitations of 2D materials for SERS application.

Graphene possesses a chemically inert and biocompatible surface and it has a few intrinsic Raman peaks. The large-area high-quality graphene is easily achievable by using CVD methods. Normally, the wet transfer process is widely applied to transfer graphene. However, when graphene is transferred by polymethyl methacrylate (PMMA)-assisted transfer, the PMMA residue always existed on the surface of the graphene. For h-BN, it does not react with weak acids and strong bases at ambient temperature. The chemical inertness ensures its outstanding long-term stability. So, it is applied to protect noble metals by constructing hybrid SERS substrates. For BP, it does not exhibit invasiveness and toxicity to biological tissue which makes BP an efficient SERS substrate for extended biosensing. One of the greatest advantages of BP beyond graphene is the energy gap which makes

it easier to detect light. However, BP is unstable and it rapidly oxidizes in the air. This degradation phenomenon has a severe impact on material properties. The use of SnSe₂ nanoflake arrays could effectively trap light and they have excellent sensitivity in SERS. The 2D SnSe₂ nanoflakes can be obtained by mechanical exfoliation without interstitials or defects. It cannot get large-area film even it can be synthesized by using CVD methods. This limitation restricts the application of SnSe₂. For MoS₂, it can be mechanically exfoliated into a single-layer structure. Additionally, the MoS₂ nanostructure can be synthesized by using chemical methods which enlarge the application of MoS₂. WS₂ can be simply prepared. WS₂ with high quality and large surface area can be obtained by using the thermal decomposition of (NH₄)₂WS₄ with two annealing processes. WS₂ has a low Mohs' hardness scale and is easily formed into a transfer film. However, the film formation state of the WS₂ coating on the metal substrate is not as good as that of the MoS₂ coating. In summary, 2D materials are important in SERS due to their unique property. For different applications, the proper 2D materials should be selected. By applying 2D materials, the SERS performances of hybrid metallic structures combining with 2D materials are improved.

5. Perspective and Conclusions

2D materials with atomic or few atomic thickness properties, unique optic, and electric properties have been widely applied in SERS. Due to the charge transfer process between the 2D materials and the molecules, 2D materials have a strong SERS enhancement of 10–100. Except for their intrinsic SERS-enhanced properties, the combination of 2D materials with kinds of metallic nanostructure is the prominent category in developing SERS substrates with high performance. The atomic composites in 2D material can interact with the metal ions and the metal NPs can be directly grown on 2D materials by using a reduction reaction. Further, the pre-fabricated metal NPs can be modified or drop-casted on 2D materials by utilizing binding molecules. The physical methods are another optional way to fabricate metal NPs or nanostructures. Thermally treating metal thin films is the most commonly used way of synthesizing metal NPs. The photolithograph and mask are used in generating metal nanodiscs, nanoholes, nano triangles et. al. The 2D material can be transferred on such metal nanostructures or directly deposited metal nanostructures on 2D material to form metallic structure/2D material system or 2D material/metallic structure. The 3D SERS substrate also can be constructed based on methods of constructing 2D material/metallic structures.

SERS is a powerful vibrational spectroscopy technique that enables the highly sensitive structural detection of analytes at low concentrations. Selectivity, reversibility, and reusability of substrates have been major issues in the field of SERS for low-concentration analytes. SERS signal enhancement depends on a good substrate. In this review, the recent strategies in the design and fabricating of new types of SERS substrates combining with 2D materials are illustrated. A brief overview of the hybrid SERS system formed by metallic nanostructure and 2D materials, ranging from traditional 2D SERS structures to advanced 3D SERS structures, has been highlighted. The SERS performance of different 2D materials-based SERS substrates is collected in Table 1. The discovery of 2D material makes it possible to integrate kinds of metallic nanostructures to form an extremely high SERS performance substrate with kinds of architectures. Owing to their large surface area, strong charge–transfer process, atomic thickness, soft, good biocompatibility, and transparency, 2D materials are widely applied in forming 2D or 3D SERS substrates. The atomic thicknesses of 2D materials make them an ideal material for generating the small gaps between coherent metallic nanostructures which can result in extremely high SERS performance.

Table 1. The collected EF and LOD of the SERS system combing with different 2D materials.

SERS substrates	Comprisable Structures	Detected Molecules	LOD (M)	EF	Ref.
Graphene	SiO ₂ /Si	R6G PPP Phthalocyanine CV		2 to 17	[22]
G/GNRs-VA	GNRs-VA	Rh6G CV	10 ⁻¹³ 10 ⁻⁹	7.9 × 10 ⁸	[71]
graphene Au NPs 1L-graphene-Au NPs Ag NPs 1L-graphene-Ag NPs	SiO ₂ /Si	CuPc		14 61 85 580 755	[7]
graphene/nano-disk graphene/nano-holes	nano-disk nano-holes	methylene blue		3 9	[39]
Graphene-Au nanopyramid	SiO ₂ /Si	Dopamine serotonin	10 ⁻¹⁰	2 × 10 ⁸ 2 × 10 ⁹	[27]
G/TNAs	TNAs	R6G	10 ⁻⁵		[73]
Ag NPs-G-Ag film	Ag NPs-G	R6G		130	[76]
Single Nanowire/Graphene (SNOG)	Bare Au film	CuPc		1.18 × 10 ⁶	[77]
3D Au NP-graphene-Ag NH array	Au NP-Ag NH array	R6G	10 ⁻¹³	137	[46]
AgNPs/bilayer graphene/Au nanonet	SiO ₂ /Si	R6G CV	10 ⁻¹³ 10 ⁻¹²	9.1 × 10 ⁹	[78]
AgNPs-graphene-AuNPs	AuNPs-graphene AgNPs-graphene	R6G CV	10 ⁻¹¹ 10 ⁻¹²		[55]
3D-AuAg ANPs/graphene/Au Ag ANPs	Graphene/AuAg ANPs	R6G	10 ⁻⁹		[79]
AuNPs-MoS ₂	MoS ₂	RhB	10 ⁻¹⁰	10 ⁴	[113]
AuNPs@MoS ₂	MoS ₂	R6G	8.2 × 10 ⁻⁷	8.2 × 10 ⁵	[112]
CF-AuNPs@ MoS ₂ -MS	MoS ₂ -MS	R6G MB	10 ⁻¹⁴ 10 ⁻¹⁵		[114]
MoS ₂ nanoflowers	MoS ₂	RhB	10 ⁻⁷		[115]
Au NP-MoS ₂ NF	MoS ₂ NF	R6G	10 ⁻¹²	10 ⁹	[116]
AuNPs/MoS ₂ /graphene vdW	AuNPs/graphene/MoS ₂	R6G	5 × 10 ⁻⁸ (633 nm laser) 5 × 10 ⁻¹⁰ (532 nm laser)		[125]
AuNPs/h-BN/Ag NPs	h-BN/Ag NPs	R6G	10 ⁻¹²	9.35 × 10 ⁷	[81]
h-BN/Ag NPs	Ag NPs	R6G	10 ⁻⁹		[82]
Au-h-BN	h-BN	R6G	10 ⁻⁹		[83]
CuPc@HG@BN	CuPc@SiO ₂	CuPc	7 × 10 ⁻¹³	7.42 × 10 ⁴	[84]
BP-AuNPs	Au NPs	CV in HepG ₂ cells	—	70	[91]
BP-Au NSs	BP NSs	tumor tissue molecular	—	2.5	[99]
AuNPs/WS ₂ @AuNPs	WS ₂ @AuNPs	R6G	10 ⁻¹¹	147.7	[124]
SnSe ₂	SiO ₂ /Si	crystal violet (CV)	10 ⁻⁷		[100]
AuNP/WS ₂ -ND/graphene	WS ₂ -ND/graphene	R6G	10 ⁻¹²	2.0	[63]
Ag@WS ₂ QD	WS ₂ QDs	malachite green (MG)		7.2 × 10 ⁵	[121]
Au NPs-WS ₂	WS ₂	R6G		65.1	[122,123]

Until now, reliable and high EF SERS substrates are still a research topic that needs to be made effort. As related research develops, 2D materials show excellent SERS performance with huge potential to replace the current commercial substrates. we can expect that 2D materials will eventually become the next generation substrates for SERS. We hope, the topic in this review can act as a steppingstone for readers and help readers to figure out some new interesting categories in fabricating 2D materials-based SERS substrates with high performance.

Author Contributions: Writing—original draft preparation, Y.L.; writing—review and editing, Y.L., Z.Q., J.D., J.Z., X.J., G.W. and F.L.; funding acquisition, Y.L. and G.W.; supervision, Y.L. and F.L. All authors have read and agreed to the published version of the manuscript.

Funding: This work has been supported by the Guangxi Natural Science Foundation Project (No. 2021GXNSFBA196049, Y.L.), Guangxi Science and Technology Project (No. AD22035215, Y.L.), the National Key Research and Development Program of China (No. 2021YFA0715404, G.W.), and Guangxi Key Research and Development Program (No. 2021AB05083, G.W.).

Institutional Review Board Statement: Not applicable.

Informed Consent Statement: Not applicable.

Data Availability Statement: Not applicable.

Conflicts of Interest: The authors declare no conflict of interest.

References

1. Brand, J. The discovery of the Raman effect. *Notes Rec. R. Soc. Lond.* **1989**, *43*, 1–23.
2. Raman, C.V. A new radiation. *Indian J. Phys.* **1928**, *2*, 387–398. [[CrossRef](#)]
3. Krishnan, R.; Shankar, R. Raman effect: History of the discovery. *J. Raman Spectrosc.* **1981**, *10*, 1–8. [[CrossRef](#)]
4. Liu, L.; Shao, M.; Cheng, L.; Zhuo, S.; Que, R.; Lee, S.T. Edge-enhanced Raman scattering effect from Au deposited nanoedge array. *Appl. Phys. Lett.* **2011**, *98*, 073114. [[CrossRef](#)]
5. Fan, M.; Andrade, G.F.S.; Brolo, A.G. A review on recent advances in the applications of surface-enhanced Raman scattering in analytical chemistry. *Anal. Chim. Acta* **2020**, *1097*, 1–29. [[CrossRef](#)]
6. Schedin, F.; Lidorikis, E.; Lombardo, A.; Kravets, V.G.; Geim, A.K.; Grigorenko, A.N.; Novoselov, K.S.; Ferrari, A.C. Surface-enhanced Raman spectroscopy of graphene. *ACS Nano* **2010**, *4*, 5617–5626. [[CrossRef](#)]
7. Xu, W.; Ling, X.; Xiao, J.; Dresselhaus, M.S.; Kong, J.; Xu, H.; Liu, Z.; Zhang, J. Surface enhanced Raman spectroscopy on a flat graphene surface. *Proc. Natl. Acad. Sci. USA* **2012**, *109*, 9281–9286. [[CrossRef](#)]
8. Reokrungruang, P.; Chatnuntawech, I.; Dharakul, T.; Bamrungrasap, S. A simple paper-based surface enhanced Raman scattering (SERS) platform and magnetic separation for cancer screening. *Sens. Actuators B: Chem.* **2019**, *285*, 462–469. [[CrossRef](#)]
9. Bamrungrasap, S.; Treerattrakul, K. Development of SERS based biosensor for cancer screening. *Asian J. Med. Biomed.* **2018**, *28*.
10. Mosier-Boss, P. Review of SERS substrates for chemical sensing. *Nanomaterials* **2017**, *7*, 142. [[CrossRef](#)]
11. Huang, W.E.; Li, M.; Jarvis, R.M.; Goodacre, R.; Banwart, S.A. Shining light on the microbial world: The application of Raman microspectroscopy. In *Advances in Applied Microbiology*; Elsevier: Amsterdam, The Netherlands, 2010; Volume 70, pp. 153–186.
12. Fleischmann, M.; Hendra, P.; McQuillan, A. RAMAN SPECTRA OF PYRIDINE ADSORBED AT A SILVER ELEC. *Chem. Phys. Lett.* **1974**, *26*, 163–166. [[CrossRef](#)]
13. Langer, J.; Jimenez de Aberasturi, D.; Aizpurua, J.; Alvarez-Puebla, R.A.; Auguie, B.; Baumberg, J.J.; Bazan, G.C.; Bell, S.E.J.; Boisen, A.; Brolo, A.G.; et al. Present and Future of Surface-Enhanced Raman Scattering. *ACS Nano* **2020**, *14*, 28–117. [[CrossRef](#)]
14. Albrecht, M.G.; Creighton, J.A. Anomalously intense Raman spectra of pyridine at a silver electrode. *J. Am. Chem. Soc.* **1977**, *99*, 5215–5217. [[CrossRef](#)]
15. Jeanmaire, D.L.; Van Duyne, R.P. Surface Raman spectroelectrochemistry: Part I. Heterocyclic, aromatic, and aliphatic amines adsorbed on the anodized silver electrode. *J. Electroanal. Chem. Interfacial Electrochem.* **1977**, *84*, 1–20. [[CrossRef](#)]
16. Le Ru, E.C.; Etchegoin, P.G. Single-molecule surface-enhanced Raman spectroscopy. *Annu. Rev. Phys. Chem.* **2012**, *63*, 65–87. [[CrossRef](#)]
17. Willets, K.A. Super-resolution imaging of SERS hot spots. *Chem. Soc. Rev.* **2014**, *43*, 3854–3864. [[CrossRef](#)]
18. Ling, X.; Huang, S.; Deng, S.; Mao, N.; Kong, J.; Dresselhaus, M.S.; Zhang, J. Lighting up the Raman signal of molecules in the vicinity of graphene related materials. *Acc. Chem. Res.* **2015**, *48*, 1862–1870. [[CrossRef](#)]
19. Xu, S.; Jiang, S.; Wang, J.; Wei, J.; Yue, W.; Ma, Y. Graphene isolated Au nanoparticle arrays with high reproducibility for high-performance surface-enhanced Raman scattering. *Sens. Actuators B: Chem.* **2016**, *222*, 1175–1183. [[CrossRef](#)]
20. Nie, S.; Emory, S.R. Probing single molecules and single nanoparticles by surface-enhanced Raman scattering. *Science* **1997**, *275*, 1102–1106. [[CrossRef](#)]
21. Huang, X.; El-Sayed, I.H.; Qian, W.; El-Sayed, M.A. Cancer cell imaging and photothermal therapy in the near-infrared region by using gold nanorods. *J. Am. Chem. Soc.* **2006**, *128*, 2115–2120. [[CrossRef](#)]
22. Ling, X.; Xie, L.; Fang, Y.; Xu, H.; Zhang, H.; Kong, J.; Dresselhaus, M.S.; Zhang, J.; Liu, Z. Can graphene be used as a substrate for Raman enhancement? *Nano Lett.* **2010**, *10*, 553–561. [[CrossRef](#)] [[PubMed](#)]
23. Chourpa, I.; Lei, F.H.; Dubois, P.; Manfait, M.; Sockalingum, G.D. Intracellular applications of analytical SERS spectroscopy and multispectral imaging. *Chem. Soc. Rev.* **2008**, *37*, 993–1000. [[CrossRef](#)] [[PubMed](#)]
24. Otto, A.; Mrozek, I.; Grabhorn, H.; Akemann, W. Surface-enhanced Raman scattering. *J. Phys. Condens. Matter* **1992**, *4*, 1143. [[CrossRef](#)]
25. Balandin, A.A.; Ghosh, S.; Bao, W.; Calizo, I.; Teweldebrhan, D.; Miao, F.; Lau, C.N. Superior thermal conductivity of single-layer graphene. *Nano Lett.* **2008**, *8*, 902–907. [[CrossRef](#)] [[PubMed](#)]
26. Jones, M.R.; Osberg, K.D.; Macfarlane, R.J.; Langille, M.R.; Mirkin, C.A. Templated techniques for the synthesis and assembly of plasmonic nanostructures. *Chem. Rev.* **2011**, *111*, 3736–3827. [[CrossRef](#)]

27. Wang, P.; Xia, M.; Liang, O.; Sun, K.; Cipriano, A.F.; Schroeder, T.; Liu, H.; Xie, Y.H. Label-Free SERS Selective Detection of Dopamine and Serotonin Using Graphene-Au Nanopyramid Heterostructure. *Anal. Chem.* **2015**, *87*, 10255–10261. [[CrossRef](#)]
28. Mu, C.; Zhang, J.P.; Xu, D. Au nanoparticle arrays with tunable particle gaps by template-assisted electroless deposition for high performance surface-enhanced Raman scattering. *Nanotechnology* **2010**, *21*, 015604. [[CrossRef](#)]
29. Du, Y.; Zhao, Y.; Qu, Y.; Chen, C.-H.; Chen, C.-M.; Chuang, C.-H.; Zhu, Y. Enhanced light-matter interaction of graphene-gold nanoparticle hybrid films for high-performance SERS detection. *J. Mater. Chem. C* **2014**, *2*, 4683–4691. [[CrossRef](#)]
30. Xu, W.; Xiao, J.; Chen, Y.; Chen, Y.; Ling, X.; Zhang, J. Graphene-veiled gold substrate for surface-enhanced Raman spectroscopy. *Adv. Mater.* **2013**, *25*, 928–933. [[CrossRef](#)]
31. Tao, L.; Li, Z.; Chen, K.; Zhou, Y.; Li, H.; Wang, X.; Zhan, R.; Hou, X.; Zhao, Y.; Xu, J.; et al. A spontaneously formed plasmonic-MoTe₂ hybrid platform for ultrasensitive Raman enhancement. *Cell Rep. Phys. Sci.* **2021**, *2*, 100506. [[CrossRef](#)]
32. Huang, Z.; Meng, G.; Huang, Q.; Yang, Y.; Zhu, C.; Tang, C. Improved SERS performance from Au nanopillar arrays by abridging the pillar tip spacing by Ag sputtering. *Adv. Mater.* **2010**, *22*, 4136–4139. [[CrossRef](#)] [[PubMed](#)]
33. Sivashanmugan, K.; Liao, J.D.; Liu, B.H.; Yao, C.K. Focused-ion-beam-fabricated Au nanorods coupled with Ag nanoparticles used as surface-enhanced Raman scattering-active substrate for analyzing trace melamine constituents in solution. *Anal. Chim. Acta* **2013**, *800*, 56–64. [[CrossRef](#)] [[PubMed](#)]
34. Sivashanmugan, K.; Liao, J.D.; Shao, P.L.; Liu, B.H.; Tseng, T.Y.; Chang, C.Y. Intense Raman scattering on hybrid Au/Ag nanopillars for the distinction of MMP-9-digested collagen type-I fiber detection. *Biosens. Bioelectron.* **2015**, *72*, 61–70. [[CrossRef](#)] [[PubMed](#)]
35. Kravets, V.G.; Schedin, F.; Jalil, R.; Britnell, L.; Novoselov, K.S.; Grigorenko, A.N. Surface Hydrogenation and Optics of a Graphene Sheet Transferred onto a Plasmonic Nanoarray. *J. Phys. Chem. C* **2012**, *116*, 3882–3887. [[CrossRef](#)]
36. Ebbesen, T.W.; Lezec, H.J.; Ghaemi, H.; Thio, T.; Wolff, P.A. Extraordinary optical transmission through sub-wavelength hole arrays. *Nature* **1998**, *391*, 667–669. [[CrossRef](#)]
37. Liu, Y.; Feng, H.; Luo, F. Quantitative analysis of the defects in CVD grown graphene by plasmon-enhanced Raman scattering. *Carbon* **2020**, *161*, 153–161. [[CrossRef](#)]
38. Yu, Q.; Guan, P.; Qin, D.; Golden, G.; Wallace, P.M. Inverted Size-Dependence of Surface-Enhanced Raman Scattering on Gold Nanohole and Nanodisk Arrays. *Nano Lett.* **2008**, *8*, 1923–1928. [[CrossRef](#)]
39. Hao, Q.; Wang, B.; Bossard, J.A.; Kiraly, B.; Zeng, Y.; Chiang, I.K.; Jensen, L.; Werner, D.H.; Huang, T.J. Surface-Enhanced Raman Scattering Study on Graphene-Coated Metallic Nanostructure Substrates. *J. Phys. Chem. C* **2012**, *116*, 7249–7254. [[CrossRef](#)]
40. Wang, P.; Zhang, W.; Liang, O.; Pantoja, M.; Katzer, J.; Schroeder, T.; Xie, Y.-H. Giant optical response from graphene-plasmonic system. *Acs Nano* **2012**, *6*, 6244–6249. [[CrossRef](#)]
41. McCreery, R.L. *Raman Spectroscopy for Chemical Analysis*; John Wiley & Sons: Hoboken, NJ, USA, 2005; Volume 225.
42. Ferraro, J.R. *Introductory Raman Spectroscopy*; Elsevier: Amsterdam, The Netherlands, 2003.
43. Colthup, N. *Introduction to Infrared and Raman Spectroscopy*; Elsevier: Amsterdam, The Netherlands, 2012.
44. Yang, S.; Dai, X.; Stogin, B.B.; Wong, T.-S. Ultrasensitive surface-enhanced Raman scattering detection in common fluids. *Proc. Natl. Acad. Sci. USA* **2016**, *113*, 268–273. [[CrossRef](#)]
45. Fan, W.; Lee, Y.H.; Pedireddy, S.; Zhang, Q.; Liu, T.; Ling, X.Y. Graphene oxide and shape-controlled silver nanoparticle hybrids for ultrasensitive single-particle surface-enhanced Raman scattering (SERS) sensing. *Nanoscale* **2014**, *6*, 4843–4851. [[CrossRef](#)] [[PubMed](#)]
46. Zhao, Y.; Yang, D.; Li, X.; Liu, Y.; Hu, X.; Zhou, D.; Lu, Y. Toward highly sensitive surface-enhanced Raman scattering: The design of a 3D hybrid system with monolayer graphene sandwiched between silver nanohole arrays and gold nanoparticles. *Nanoscale* **2017**, *9*, 1087–1096. [[CrossRef](#)] [[PubMed](#)]
47. Grand, J.; de La Chapelle, M.L.; Bijeon, J.-L.; Adam, P.-M.; Vial, A.; Royer, P. Role of localized surface plasmons in surface-enhanced Raman scattering of shape-controlled metallic particles in regular arrays. *Phys. Rev. B* **2005**, *72*, 033407. [[CrossRef](#)]
48. Haynes, C.L.; Van Duyne, R.P. Plasmon-sampled surface-enhanced Raman excitation spectroscopy. *J. Phys. Chem. B* **2003**, *107*, 7426–7433. [[CrossRef](#)]
49. McFarland, A.D.; Young, M.A.; Dieringer, J.A.; Van Duyne, R.P. Wavelength-scanned surface-enhanced Raman excitation spectroscopy. *J. Phys. Chem. B* **2005**, *109*, 11279–11285. [[CrossRef](#)]
50. Morton, S.M.; Jensen, L. Understanding the Molecule–Surface Chemical Coupling in SERS. *J. Am. Chem. Soc.* **2009**, *131*, 4090–4098. [[CrossRef](#)]
51. Sarau, G.; Lahiri, B.; Banzer, P.; Gupta, P.; Bhattacharya, A.; Vollmer, F.; Christiansen, S. Enhanced Raman scattering of graphene using arrays of split ring resonators. *Adv. Opt. Mater.* **2013**, *1*, 151–157. [[CrossRef](#)]
52. Yuk, J.M.; Kim, K.; Alemán, B.; Regan, W.; Ryu, J.H.; Park, J.; Ercius, P.; Lee, H.M.; Alivisatos, A.P.; Crommie, M.F. Graphene veils and sandwiches. *Nano Lett.* **2011**, *11*, 3290–3294. [[CrossRef](#)]
53. Huang, X.; Yin, Z.; Wu, S.; Qi, X.; He, Q.; Zhang, Q.; Yan, Q.; Boey, F.; Zhang, H. Graphene-based materials: Synthesis, characterization, properties, and applications. *Small* **2011**, *7*, 1876–1902. [[CrossRef](#)]
54. Li, Y.; Dykes, J.; Gilliam, T.; Chopra, N. A new heterostructured SERS substrate: Free-standing silicon nanowires decorated with graphene-encapsulated gold nanoparticles. *Nanoscale* **2017**, *9*, 5263–5272. [[CrossRef](#)]
55. Zhang, C.; Li, C.; Yu, J.; Jiang, S.; Xu, S.; Yang, C.; Liu, Y.J.; Gao, X.; Liu, A.; Man, B. SERS activated platform with three-dimensional hot spots and tunable nanometer gap. *Sens. Actuators B: Chem.* **2018**, *258*, 163–171. [[CrossRef](#)]

56. Joo, Y.; Kim, M.; Kanimozhi, C.; Huang, P.; Wong, B.M.; Singha Roy, S.; Arnold, M.S.; Gopalan, P. Effect of Dipolar Molecule Structure on the Mechanism of Graphene-Enhanced Raman Scattering. *J. Phys. Chem. C* **2016**, *120*, 13815–13824. [[CrossRef](#)]
57. Liu, Y.; Hu, Y.; Zhang, J. Few-Layer Graphene-Encapsulated Metal Nanoparticles for Surface-Enhanced Raman Spectroscopy. *J. Phys. Chem. C* **2014**, *118*, 8993–8998. [[CrossRef](#)]
58. Fu, X.; Wang, Y.; Liu, Y.; Liu, H.; Fu, L.; Wen, J.; Li, J.; Wei, P.; Chen, L. A graphene oxide/gold nanoparticle-based amplification method for SERS immunoassay of cardiac troponin I. *Analyst* **2019**, *144*, 1582–1589. [[CrossRef](#)]
59. Nair, R.V.; Murukeshan, V.M. (Cu 2 O-Au)–Graphene-Au layered structures as efficient near Infra-Red SERS substrates. *Sci. Rep.* **2020**, *10*, 4152. [[CrossRef](#)]
60. Xie, L.; Ling, X.; Fang, Y.; Zhang, J.; Liu, Z. Graphene as a Substrate To Suppress Fluorescence in Resonance Raman Spectroscopy. *J. Am. Chem. Soc.* **2009**, *131*, 9890–9891. [[CrossRef](#)]
61. Thrall, E.S.; Crowther, A.C.; Yu, Z.; Brus, L.E. R6G on graphene: High Raman detection sensitivity, yet decreased Raman cross-section. *Nano Lett.* **2012**, *12*, 1571–1577. [[CrossRef](#)]
62. Cao, Z.; He, P.; Huang, T.; Yang, S.; Han, S.; Wang, X.; Ding, G. Plasmonic Coupling of AgNPs near Graphene Edges: A Cross-Section Strategy for High-Performance SERS Sensing. *Chem. Mater.* **2020**, *32*, 3813–3822. [[CrossRef](#)]
63. Ghopry, S.A.; Alamri, M.; Goul, R.; Cook, B.; Sadeghi, S.M.; Gutha, R.R.; Sakidja, R.; Wu, J.Z. Au Nanoparticle/WS₂ Nanodome/Graphene van der Waals Heterostructure Substrates for Surface-Enhanced Raman Spectroscopy. *ACS Appl. Nano Mater.* **2020**, *3*, 2354–2363. [[CrossRef](#)]
64. Lin, P.Y.; Hsieh, C.W.; Hsieh, S. Rapid and Sensitive SERS Detection of Bisphenol A Using Self-assembled Graphitic Substrates. *Sci. Rep.* **2017**, *7*, 16698. [[CrossRef](#)]
65. Vales, V.; Drogowska-Horna, K.; Guerra, V.L.P.; Kalbac, M. Graphene-enhanced Raman scattering on single layer and bilayers of pristine and hydrogenated graphene. *Sci. Rep.* **2020**, *10*, 4516. [[CrossRef](#)]
66. Li, Z.; Ye, L.; Wang, Y.; Xu, S.; Lei, F.; Lin, S. Visible light assisted electro-photo synergistic catalysis of heterostructured Pd–Ag NPs/graphene for methanol oxidation. *RSC Adv.* **2016**, *6*, 79533–79541. [[CrossRef](#)]
67. Pérez, L.A.; Dalfovo, M.C.; Troiani, H.; Soldati, A.L.; Lacconi, G.I.; Ibañez, F.J. CVD graphene transferred with Au nanoparticles: An ideal platform for TERS and SERS on a single triangular nanoplate. *J. Phys. Chem. C* **2016**, *120*, 8315–8322. [[CrossRef](#)]
68. Dalfovo, M.C.; Lacconi, G.I.; Moreno, M.n.; Yappert, M.C.; Sumanasekera, G.U.; Salvarezza, R.C.; Ibañez, F.J. Synergy between graphene and au nanoparticles (heterojunction) towards quenching, improving raman signal, and UV light sensing. *ACS Appl. Mater. Interfaces* **2014**, *6*, 6384–6391. [[CrossRef](#)] [[PubMed](#)]
69. Liang, X.; Liang, B.; Pan, Z.; Lang, X.; Zhang, Y.; Wang, G.; Yin, P.; Guo, L. Tuning plasmonic and chemical enhancement for SERS detection on graphene-based Au hybrids. *Nanoscale* **2015**, *7*, 20188–20196. [[CrossRef](#)] [[PubMed](#)]
70. Liu, Y.; Luo, F. Large-scale highly ordered periodic Au nano-discs/graphene and graphene/Au nanoholes plasmonic substrates for surface-enhanced Raman scattering. *Nano Res.* **2019**, *12*, 2788–2795. [[CrossRef](#)]
71. Zhao, X.; Dong, J.; Cao, E.; Han, Q.; Gao, W.; Wang, Y.; Qi, J.; Sun, M. Plasmon-exciton coupling by hybrids between graphene and gold nanorods vertical array for sensor. *Appl. Mater. Today* **2019**, *14*, 166–174. [[CrossRef](#)]
72. Nikoobakht, B.; El-Sayed, M.A. Preparation and growth mechanism of gold nanorods (NRs) using seed-mediated growth method. *Chem. Mater.* **2003**, *15*, 1957–1962. [[CrossRef](#)]
73. Zhang, X.; Si, S.; Zhang, X.; Wu, W.; Xiao, X.; Jiang, C. Improved Thermal Stability of Graphene-Veiled Noble Metal Nanoarrays as Recyclable SERS Substrates. *ACS Appl. Mater. Interfaces* **2017**, *9*, 40726–40733. [[CrossRef](#)]
74. Ko, H.; Singamaneni, S.; Tsukruk, V.V. Nanostructured surfaces and assemblies as SERS media. *Small* **2008**, *4*, 1576–1599. [[CrossRef](#)]
75. Kodyath, R.; Malak, S.T.; Combs, Z.A.; Koenig, T.; Mahmoud, M.A.; El-Sayed, M.A.; Tsukruk, V.V. Assemblies of silver nanocubes for highly sensitive SERS chemical vapor detection. *J. Mater. Chem. A* **2013**, *1*, 2777–2788. [[CrossRef](#)]
76. Li, X.; Choy, W.C.; Ren, X.; Zhang, D.; Lu, H. Highly intensified surface enhanced Raman scattering by using monolayer graphene as the nanospacer of metal film–metal nanoparticle coupling system. *Adv. Funct. Mater.* **2014**, *24*, 3114–3122. [[CrossRef](#)]
77. Kim, H.; Seol, M.-L.; Lee, D.-I.; Lee, J.; Kang, I.-S.; Lee, H.; Kang, T.; Choi, Y.-K.; Kim, B. Single nanowire on graphene (SNOG) as an efficient, reproducible, and stable SERS-active platform. *Nanoscale* **2016**, *8*, 8878–8886. [[CrossRef](#)] [[PubMed](#)]
78. Li, C.; Zhang, C.; Xu, S.; Huo, Y.; Jiang, S.; Yang, C.; Li, Z.; Zhao, X.; Zhang, S.; Man, B. Experimental and theoretical investigation for a hierarchical SERS activated platform with 3D dense hot spots. *Sens. Actuators B Chem.* **2018**, *263*, 408–416. [[CrossRef](#)]
79. Han, Q.; Lu, Z.; Gao, W.; Wu, M.; Wang, Y.; Wang, Z.; Qi, J.; Dong, J. Three-dimensional AuAg alloy NPs/graphene/AuAg alloy NP sandwiched hybrid nanostructure for surface enhanced Raman scattering properties. *J. Mater. Chem. C* **2020**, *8*, 12599–12606. [[CrossRef](#)]
80. Ling, X.; Fang, W.; Lee, Y.H.; Araujo, P.T.; Zhang, X.; Rodriguez-Nieva, J.F.; Lin, Y.; Zhang, J.; Kong, J.; Dresselhaus, M.S. Raman enhancement effect on two-dimensional layered materials: Graphene, h-BN and MoS₂. *Nano Lett.* **2014**, *14*, 3033–3040. [[CrossRef](#)]
81. Kim, N.Y.; Leem, Y.C.; Hong, S.H.; Park, J.H.; Yim, S.Y. Ultrasensitive and Stable Plasmonic Surface-Enhanced Raman Scattering Substrates Covered with Atomically Thin Monolayers: Effect of the Insulating Property. *ACS Appl. Mater. Interfaces* **2019**, *11*, 6363–6373. [[CrossRef](#)]
82. Chugh, D.; Jagadish, C.; Tan, H. Large-Area Hexagonal Boron Nitride for Surface Enhanced Raman Spectroscopy. *Adv. Mater. Technol.* **2019**, *4*, 1900220. [[CrossRef](#)]

83. Kim, G.; Kim, M.; Hyun, C.; Hong, S.; Ma, K.Y.; Shin, H.S.; Lim, H. Hexagonal Boron Nitride/Au Substrate for Manipulating Surface Plasmon and Enhancing Capability of Surface-Enhanced Raman Spectroscopy. *ACS Nano* **2016**, *10*, 11156–11162. [[CrossRef](#)]
84. Liu, J.; Zheng, T.; Tian, Y. Functionalized h-BN Nanosheets as a Theranostic Platform for SERS Real-Time Monitoring of MicroRNA and Photodynamic Therapy. *Angew. Chem.* **2019**, *131*, 7839–7843. [[CrossRef](#)]
85. Cui, S.; Pu, H.; Wells, S.A.; Wen, Z.; Mao, S.; Chang, J.; Hersam, M.C.; Chen, J. Ultrahigh sensitivity and layer-dependent sensing performance of phosphorene-based gas sensors. *Nat. Commun.* **2015**, *6*, 8632. [[CrossRef](#)] [[PubMed](#)]
86. Yasaei, P.; Behranginia, A.; Foroozan, T.; Asadi, M.; Kim, K.; Khalili-Araghi, F.; Salehi-Khojin, A. Stable and Selective Humidity Sensing Using Stacked Black Phosphorus Flakes. *ACS Nano* **2015**, *9*, 9898–9905. [[CrossRef](#)] [[PubMed](#)]
87. Cho, S.Y.; Lee, Y.; Koh, H.J.; Jung, H.; Kim, J.S.; Yoo, H.W.; Kim, J.; Jung, H.T. Superior Chemical Sensing Performance of Black Phosphorus: Comparison with MoS₂ and Graphene. *Adv. Mater.* **2016**, *28*, 7020–7028. [[CrossRef](#)] [[PubMed](#)]
88. Ling, X.; Wang, H.; Huang, S.; Xia, F.; Dresselhaus, M.S. The renaissance of black phosphorus. *Proc. Natl. Acad. Sci. USA* **2015**, *112*, 4523–4530. [[CrossRef](#)]
89. Liu, H.; Du, Y.; Deng, Y.; Ye, P.D. Semiconducting black phosphorus: Synthesis, transport properties and electronic applications. *Chem Soc Rev* **2015**, *44*, 2732–2743. [[CrossRef](#)]
90. Li, L.; Yu, Y.; Ye, G.J.; Ge, Q.; Ou, X.; Wu, H.; Feng, D.; Chen, X.H.; Zhang, Y. Black phosphorus field-effect transistors. *Nat. Nanotechnol.* **2014**, *9*, 372–377. [[CrossRef](#)]
91. Liu, Z.; Chen, H.; Jia, Y.; Zhang, W.; Zhao, H.; Fan, W.; Zhang, W.; Zhong, H.; Ni, Y.; Guo, Z. A two-dimensional fingerprint nanoprobe based on black phosphorus for bio-SERS analysis and chemo-photothermal therapy. *Nanoscale* **2018**, *10*, 18795–18804. [[CrossRef](#)]
92. Shao, J.; Xie, H.; Huang, H.; Li, Z.; Sun, Z.; Xu, Y.; Xiao, Q.; Yu, X.-F.; Zhao, Y.; Zhang, H.; et al. Biodegradable black phosphorus-based nanospheres for in vivo photothermal cancer therapy. *Nat. Commun.* **2016**, *7*, 12967. [[CrossRef](#)]
93. Sun, C.; Wen, L.; Zeng, J.; Wang, Y.; Sun, Q.; Deng, L.; Zhao, C.; Li, Z. One-pot solventless preparation of PEGylated black phosphorus nanoparticles for photoacoustic imaging and photothermal therapy of cancer. *Biomaterials* **2016**, *91*, 81–89. [[CrossRef](#)]
94. Mao, C.; Xiang, Y.; Liu, X.; Cui, Z.; Yang, X.; Li, Z.; Zhu, S.; Zheng, Y.; Yeung, K.W.K.; Wu, S. Repeatable Photodynamic Therapy with Triggered Signaling Pathways of Fibroblast Cell Proliferation and Differentiation To Promote Bacteria-Accompanied Wound Healing. *ACS Nano* **2018**, *12*, 1747–1759. [[CrossRef](#)]
95. Wang, H.; Yang, X.; Shao, W.; Chen, S.; Xie, J.; Zhang, X.; Wang, J.; Xie, Y. Ultrathin Black Phosphorus Nanosheets for Efficient Singlet Oxygen Generation. *J. Am. Chem. Soc.* **2015**, *137*, 11376–11382. [[CrossRef](#)] [[PubMed](#)]
96. Geng, S.; Wu, L.; Cui, H.; Tan, W.; Chen, T.; Chu, P.K.; Yu, X.F. Synthesis of lipid-black phosphorus quantum dot bilayer vesicles for near-infrared-controlled drug release. *Chem. Commun.* **2018**, *54*, 6060–6063. [[CrossRef](#)] [[PubMed](#)]
97. Tao, W.; Zhu, X.; Yu, X.; Zeng, X.; Xiao, Q.; Zhang, X.; Ji, X.; Wang, X.; Shi, J.; Zhang, H.; et al. Black Phosphorus Nanosheets as a Robust Delivery Platform for Cancer Theranostics. *Adv. Mater.* **2017**, *29*, 1603276. [[CrossRef](#)] [[PubMed](#)]
98. Zhao, H.; Zhang, W.; Liu, Z.; Huang, D.; Zhang, W.; Ye, B.; Hu, G.; Zhong, H.; Zhuang, Z.; Guo, Z. Insights into the intracellular behaviors of black-phosphorus-based nanocomposites via surface-enhanced Raman spectroscopy. *Nanophotonics* **2018**, *7*, 1651–1662. [[CrossRef](#)]
99. Yang, G.; Liu, Z.; Li, Y.; Hou, Y.; Fei, X.; Su, C.; Wang, S.; Zhuang, Z.; Guo, Z. Facile synthesis of black phosphorus-Au nanocomposites for enhanced photothermal cancer therapy and surface-enhanced Raman scattering analysis. *Biomater. Sci.* **2017**, *5*, 2048–2055. [[CrossRef](#)]
100. Liu, M.; Shi, Y.; Wu, M.; Tian, Y.; Wei, H.; Sun, Q.; Shafi, M.; Man, B. UV surface-enhanced Raman scattering properties of SnSe₂ nanoflakes. *J. Raman Spectrosc.* **2020**, *51*, 750–755. [[CrossRef](#)]
101. Ren, B.; Lin, X.-F.; Yang, Z.-L.; Liu, G.-K.; Aroca, R.F.; Mao, B.-W.; Tian, Z.-Q. Surface-enhanced Raman scattering in the ultraviolet spectral region: UV-SERS on rhodium and ruthenium electrodes. *J. Am. Chem. Soc.* **2003**, *125*, 9598–9599. [[CrossRef](#)]
102. Cui, L.; Wu, D.-Y.; Wang, A.; Ren, B.; Tian, Z.-Q. Charge-transfer enhancement involved in the SERS of adenine on Rh and Pd demonstrated by ultraviolet to visible laser excitation. *J. Phys. Chem. C* **2010**, *114*, 16588–16595. [[CrossRef](#)]
103. Cui, L.; Mahajan, S.; Cole, R.; Soares, B.; Bartlett, P.; Baumberg, J.; Hayward, I.; Ren, B.; Russell, A.; Tian, Z. UV SERS at well ordered Pd sphere segment void (SSV) nanostructures. *Phys. Chem. Chem. Phys.* **2009**, *11*, 1023–1026. [[CrossRef](#)]
104. Tsoutsis, D.; Guerrini, L.; Hermida-Ramon, J.M.; Giannini, V.; Liz-Marzán, L.M.; Wei, A.; Alvarez-Puebla, R.A. Simultaneous SERS detection of copper and cobalt at ultratrace levels. *Nanoscale* **2013**, *5*, 5841–5846. [[CrossRef](#)]
105. Ding, T.; Sigle, D.O.; Herrmann, L.O.; Wolverson, D.; Baumberg, J.J. Nanoimprint lithography of Al nanovoids for deep-UV SERS. *ACS Appl. Mater. Interfaces* **2014**, *6*, 17358–17363. [[CrossRef](#)]
106. Achimovičová, M.; da Silva, K.L.; Daneu, N.; Rečnik, A.; Indris, S.; Hain, H.; Scheuermann, M.; Hahn, H.; Šepelák, V. Structural and morphological study of mechanochemically synthesized tin diselenide. *J. Mater. Chem.* **2011**, *21*, 5873–5876. [[CrossRef](#)]
107. Fang, Z.; Hao, S.; Long, L.; Fang, H.; Qiang, T.; Song, Y. The enhanced photoelectrochemical response of SnSe₂ nanosheets. *CrystEngComm* **2014**, *16*, 2404–2410. [[CrossRef](#)]
108. Novoselov, K.S.; Geim, A.K.; Morozov, S.V.; Jiang, D.; Katsnelson, M.I.; Grigorieva, I.; Dubonos, S.; Firsov, A.A. Two-dimensional gas of massless Dirac fermions in graphene. *Nature* **2005**, *438*, 197–200. [[CrossRef](#)]
109. Geim, A.K.; Novoselov, K.S. The rise of graphene. In *Nanoscience and Technology: A Collection of Reviews from Nature Journals*; World Scientific: Singapore, 2010; pp. 11–19.

110. Shimada, T.; Hamaguchi, K.; Koma, A.; Ohuchi, F. Electronic structures at the interfaces between copper phthalocyanine and layered materials. *Appl. Phys. Lett.* **1998**, *72*, 1869–1871. [[CrossRef](#)]
111. Sun, L.; Hu, H.; Zhan, D.; Yan, J.; Liu, L.; Teguh, J.S.; Yeow, E.K.; Lee, P.S.; Shen, Z. Plasma modified MoS₂ nanoflakes for surface enhanced raman scattering. *Small* **2014**, *10*, 1090–1095. [[CrossRef](#)]
112. Su, S.; Zhang, C.; Yuwen, L.; Chao, J.; Zuo, X.; Liu, X.; Song, C.; Fan, C.; Wang, L. Creating SERS hot spots on MoS₂ nanosheets with in situ grown gold nanoparticles. *ACS Appl Mater Interfaces* **2014**, *6*, 18735–18741. [[CrossRef](#)]
113. Rani, R.; Yoshimura, A.; Das, S.; Sahoo, M.R.; Kundu, A.; Sahu, K.K.; Meunier, V.; Nayak, S.K.; Koratkar, N.; Hazra, K.S. Sculpting Artificial Edges in Monolayer MoS₂ for Controlled Formation of Surface-Enhanced Raman Hotspots. *ACS Nano* **2020**, *14*, 6258–6268. [[CrossRef](#)]
114. Qiu, H.; Wang, M.; Li, L.; Li, J.; Yang, Z.; Cao, M. Hierarchical MoS₂-microspheres decorated with 3D AuNPs arrays for high-efficiency SERS sensing. *Sens. Actuators B: Chem.* **2018**, *255*, 1407–1414. [[CrossRef](#)]
115. Singh, J.; Rishikesh; Kumar, S.; Soni, R.K. Synthesis of 3D-MoS₂ nanoflowers with tunable surface area for the application in photocatalysis and SERS based sensing. *J. Alloys Compd.* **2020**, *849*, 156502. [[CrossRef](#)]
116. Singha, S.S.; Mondal, S.; Bhattacharya, T.S.; Das, L.; Sen, K.; Satpati, B.; Das, K.; Singha, A. Au nanoparticles functionalized 3D-MoS₂ nanoflower: An efficient SERS matrix for biomolecule sensing. *Biosens. Bioelectron.* **2018**, *119*, 10–17. [[CrossRef](#)] [[PubMed](#)]
117. Heine, T. Transition Metal Chalcogenides: Ultrathin Inorganic Materials with Tunable Electronic Properties. *Acc. Chem. Res.* **2015**, *48*, 65–72. [[CrossRef](#)] [[PubMed](#)]
118. Dufferwiel, S.; Lyons, T.P.; Solnyshkov, D.D.; Trichet, A.A.P.; Withers, F.; Schwarz, S.; Malpuech, G.; Smith, J.M.; Novoselov, K.S.; Skolnick, M.S.; et al. Valley-addressable polaritons in atomically thin semiconductors. *Nat. Photonics* **2017**, *11*, 497–501. [[CrossRef](#)]
119. Wang, Z.; Nan, J.; Yao, M.; Yang, Y. Effect of additional polyaluminum chloride and polyacrylamide on the evolution of floc characteristics during floc breakage and re-growth process. *Sep. Purif. Technol.* **2017**, *173*, 144–150. [[CrossRef](#)]
120. Meng, L.; Hu, S.; Xu, C.; Wang, X.; Li, H.; Yan, X. Surface enhanced Raman effect on CVD growth of WS₂ film. *Chem. Phys. Lett.* **2018**, *707*, 71–74. [[CrossRef](#)]
121. Song, Y.; Huang, H.-C.; Lu, W.; Li, N.; Su, J.; Cheng, S.-B.; Lai, Y.; Chen, J.; Zhan, J. Ag@WS₂ quantum dots for Surface Enhanced Raman Spectroscopy: Enhanced charge transfer induced highly sensitive detection of thiram from honey and beverages. *Food Chem.* **2020**, *344*, 128570. [[CrossRef](#)]
122. Sow, B.M.; Lu, J.; Liu, H.; Goh, K.E.J.; Sow, C.H. Enriched Fluorescence Emission from WS₂ Monoflake Empowered by Au Nanoexplorers. *Adv. Opt. Mater.* **2017**, *5*, 1700156. [[CrossRef](#)]
123. Abid, K.; Belkhir, N.H.; Jaber, S.B.; Zribi, R.; Donato, M.G.; Di Marco, G.; Gucciardi, P.G.; Neri, G.; Maàlej, R. Photoinduced Enhanced Raman Spectroscopy with Hybrid Au@WS₂ Nanosheets. *J. Phys. Chem. C* **2020**, *124*, 20350–20358. [[CrossRef](#)]
124. Lu, Z.; Si, H.; Li, Z.; Yu, J.; Liu, Y.; Feng, D.; Zhang, C.; Yang, W.; Man, B.; Jiang, S. Sensitive, reproducible, and stable 3D plasmonic hybrids with bilayer WS₂ as nanospacer for SERS analysis. *Opt. Express* **2018**, *26*, 21626. [[CrossRef](#)]
125. Alamri, M.; Sakidja, R.; Goul, R.; Ghopry, S.; Wu, J.Z. Plasmonic Au Nanoparticles on 2D MoS₂/Graphene van der Waals Heterostructures for High-Sensitivity Surface-Enhanced Raman Spectroscopy. *ACS Appl. Nano Mater.* **2019**, *2*, 1412–1420. [[CrossRef](#)]